2020

Copper(I) Iodide-Based Chemical Sensor Materials In Gaseous And Aqueous Media

Matthew D. Kessler
William & Mary - Arts & Sciences, mdkessler@email.wm.edu

Copper(I) Iodide-Based Chemical Sensor Materials in Gaseous and Aqueous Media

Matthew David Kessler

Clemmons, North Carolina

Roanoke College, 2016

A Thesis presented to the Graduate Faculty of The College of William & Mary in Candidacy

for the Degree of

Master of Science

Chemistry Department

College of William & Mary

August 2020

APPROVAL PAGE

This Thesis is submitted in partial fulfillment of
the requirements for the degree of

Master of Science

Matthew David Kessler

Approved by the Committee July 2020

Committee Chair
Robert Pike, Professor, Chemistry
College of William & Mary

Deborah Bebout, Professor, Chemistry
College of William & Mary

William McNamara, Associate Professor, Chemistry
College of William & Mary

ABSTRACT

Chemical detection is an area of great importance in the shift to more green approaches to industry. Some of the chemical species produced by assorted industries can be harmful, long lived, and challenging to differentiate. Copper(I) iodide (CuI) is a material that readily forms complexes of multiple colors, both under visible and ultraviolet (UV) light. The process of CuI reacting with dimethyl sulfide vapor to produce a color change (vapochromism) has been analyzed to propose mechanistic information about the process. Using the information obtained, a series of potential sensor materials were developed with CuI as the base. The complexes were synthesized using pyridine substituted with electron withdrawing groups to give compounds of the general form $(CuI)_x(X\text{-}Py)_y$. The various complexes were characterized using elemental analysis, single crystal X-Ray diffraction, and luminescence behavior. The complex $(CuI)_4(3\text{-}PyNO_2)_4$ was particularly promising as a sensing material due to its lack of emission and weak binding characteristics. This material was tested for its performance as a sensor in aqueous media in the detection of pyridine, a common industrial pollutant.

TABLE OF CONTENTS

ACKNOWLEDGEMENTS

I owe a tremendous debt of gratitude to those who have helped me on my path to this point. First and foremost I want to thank Dr. Pike for his exceptional mentorship, guidance, and instruction throughout my time at William and Mary. I cannot thank him enough for the time and effort that he committed to me. I am immensely grateful for the opportunity I had to be at William and Mary and work with Dr. Pike. I also want to thank the other faculty and staff at William and Mary for all of the help and instruction they provided. I especially want to thank Dr. McNamara and Dr. Bebout for their willingness to serve as committee members and Jeff Molloy for his advice and assistance in making sure my research could continue uninterrupted.

I would not be here if not for the contributions of others through my academic career. I want to thank Dr. Steve Hughes and the rest of the Roanoke College Chemistry Department for really starting me on the path to research and providing a foundation that has served me well. I want to thank Dr. Scott Collins for his advice and support. I have had the privilege of working with Dr. Aaron Nicholas and Dr. Dave Welch and am extremely appreciative of the advice, education, and collaboration they have provided. I want to extend my appreciation for the fellow graduate and undergraduate students I have worked with. The environment of cooperation and support they produced has helped me through this process. Last and certainly not least, I could not have achieved what I have without the unceasing love and support of my family. They have been a constant beacon of support for me and I cannot thank them enough.

LIST OF TABLES

LIST OF FIGURES

1) Introduction

Although pollution and environmental responsibility are matters of common discussion, these are multifaceted issues that require constant development in order to solve global problems. The term “pollutant” for the layman often conjures up toxic metals such as mercury, cadmium, and lead. Although these metals are legitimate environmental hazards, they by no means encompass the entirety of toxic chemical byproducts and waste produced in modern society. Also of high importance are organic pollutants. Organic pollutants are compounds that are metal-free and chiefly feature elements like carbon, hydrogen, oxygen, nitrogen, and sulfur. These compounds are ubiquitous, being associated with a wide range of industrial processes. Perhaps more troubling is the fact that organic compounds can have great longevity in water sources and biological enivronments.[1] The biological effects of organic compounds can result in acute and/or long-term toxicity. These can span the full gamut of negative effects, including targeted toxicity of organs and general damage to assorted biological systems.[2] Given the current widespread distribution of byproducts and other pollutants, it is obvious that detection and testing of water and air must be widely available, sensitive, and discriminating. The development of sensors that can do the above presents real challenges. These requirements are even more important in a time of rapid industrial development across the planet where universally available environmental testing are increasingly needed as global industry expands.

Organic Pollutants (OP) can come in a variety of structures and functions. They are formed nearly ubiquitously in assorted industrial processes, and inevitably become distributed into water and air. Environmentally relevant OP arise not only from man-made processes. There are a number of naturally produced compounds that can impact ecosystems negatively. Three examples of organic pollutants are shown below in Figure 1.1.

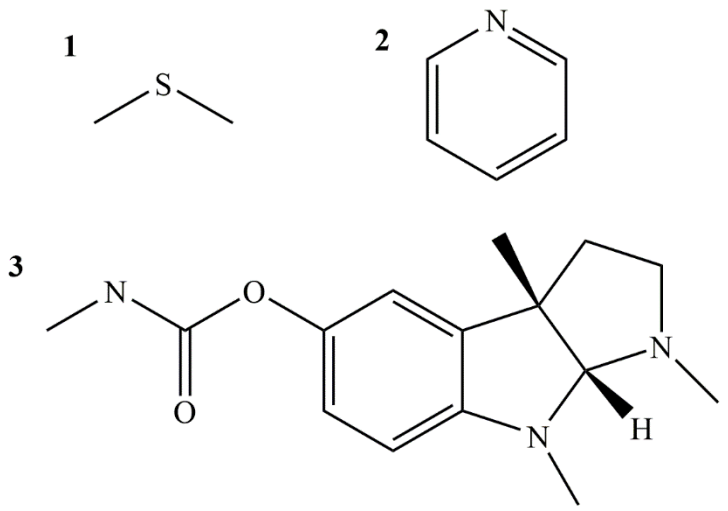

Figure 1.1: Three ecologically relevant OP molecules. 1: dimethyl sulfide (DMS), 2: pyridine, 3: physostigimine.

Figure 1.1 above is suggestive of the structural diversity range in OPs. DMS is produced biologically by a number of marine biological systems,[3] pyridine is a common industrial pollutant, and physostigimine is a pharmaceutical used to treat glaucoma. These three compounds have three different sources, but each can be ecologically harmful. Creating a method to distinguish between these and a multitude of other structurally unique organic pollutants is a legitimate challenge.

Currently one of the most popular approaches to analyzing the composition of solutions or vapor mixtures involves benchtop chemical instrumentation. Various chromatographic instruments are commonly used for chemical separations, including gas chromatography (GC), Liquid Chromatography (LC) and High Performance Liquid Chromatography (HPLC). These techniques are often paired with mass spectroscopy (MS) for chemical fingerprinting. These types of instruments can provide detailed information about the identity of many individual organic chemical components found in solution or gaseous mixtures. Such instruments generally have excellent accuracy, selectivity, and limits of detection. Despite this superb performance profile, there are downsides to relying on traditional laboratory instrumentation. Perhaps the most obvious is that the sample must be taken from the field and shipped to the laboratory for analysis. The

resulting time delay can have negative impacts, including compromised sample quality, delayed hazard recognition, and delayed hazard abatement. If the sampling needs outstrip laboratory throughput, then a backlog of samples could develop, further worsening these problems. In recent years “portable” GCMS instruments have been developed, but their cost is typically in the $100-$150K range and so may be prohibitively expensive.[4] The cost of laboratory benchtop instrumentation can also represent a challenge. Setting up lab space with dedicated instrumentation represents a significant upfront investment, which is followed by non-trivial upkeep costs. There is also significant cost associated with manning instruments with trained personnel. These drawbacks are not necessarily a problem for organizations that can front the capital, but may pose a challenge to a developing country or a business that doesn’t have a ready source of capital. Thus, while modern instrumentation is the best practice for testing quality, it suffers major drawbacks with regard to on-site use, cost, and operational requirements. These downsides can be major barriers to widespread environmental testing.

A promising avenue to solve this challenge is development of chemical sensors. These typically make use of a chemically responsive material. In this context a chemical sensor is a device that undergoes a chemical change of some kind in response to the analyte of interest to produce an observable change. A general diagram of a general chemical sensor is shown below in Figure 1.2.

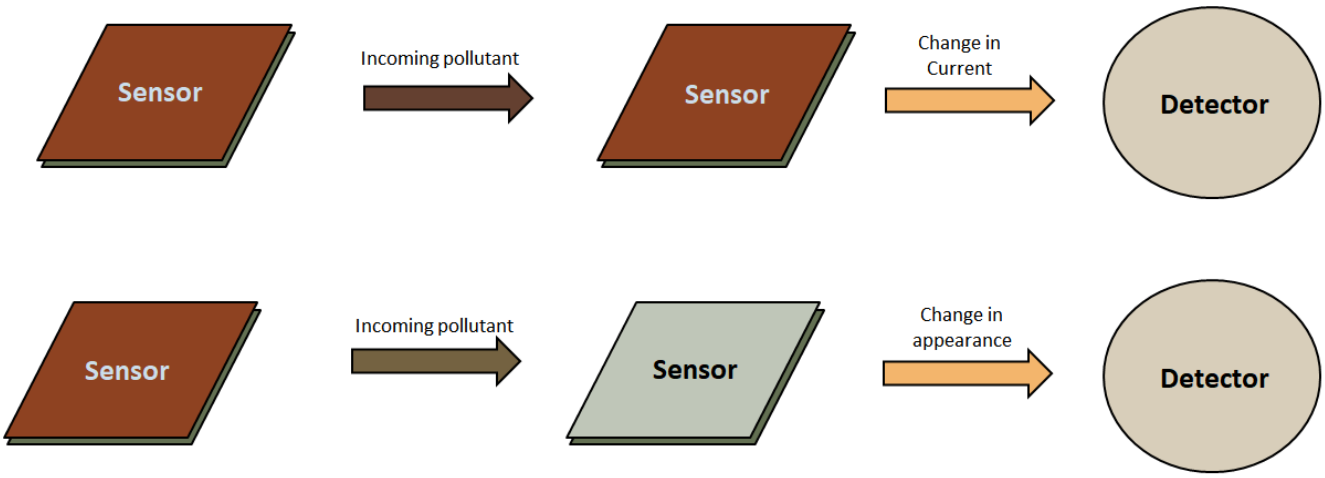

Figure 1.2: A diagram showing the design and general mechanism of action for a chemical sensor.

Ideally, a chemical would replicate many or all of the functions of traditional analytical instrumentation, but with low cost and high portability. In order for a chemical sensor to be effective, it must be sensitive and discriminating toward its target, as well as practical to use. A sensitive chemical sensor would be able to distinguish between small differences in amount for a given pollutant. It should also be able to detect its target compounds at very low levels, i.e. it should have a very low limit of detection (LOD). Often environmental pollutants are present in low concentrations and so a highly sensitive detector is needed to enable accurate distinction between low but environmentally significant concentrations.[4] A discriminating chemical sensor is one that is able to respond uniquely to one or more specific pollutants, even in the presence of chemically related compounds. As shown above in Figure 1.1, there is wide structural diversity amongst organic pollutants. Ideally, the chemical sensor would be able to distinguish between even similar structures. The differences between two or more structures might be very small, but even small structural differences can produce altered chemical properties. An example of such chemical similarities is shown below in Figure 1.3. As OP molecules get larger, structural variety can be more diverse.

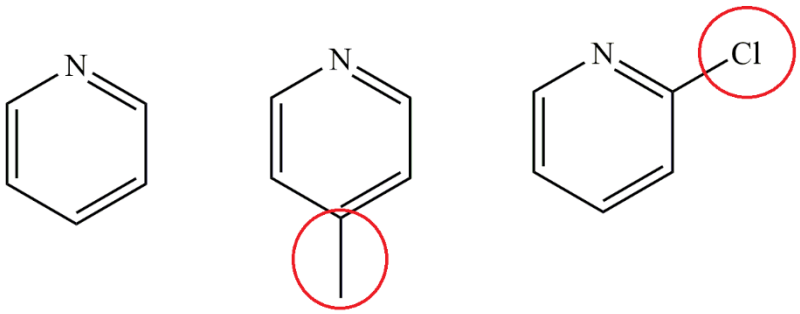

Figure 1.3: Three structures based on pyridine (far left) with small structural variations (shown in red circles).

Developing a sensing material that can distinguish between two very similar structures *and* two very different structures is a major challenge. A practical chemical sensor would be easy to use, portable, and stable under non-use conditions. If possible, it should be producible at minimal cost. Taken all together, the requirements for chemical sensing materials are daunting, but they can be overcome.

Chemical sensor materials can have varying compositions and mechanisms of action. At the broadest level there are really two types of chemical sensors. Some chemical sensors directly facilitate a measurable change in current as a result of the chemistry that has taken place.[5] Other sensors are operate on a visible color change or a change in light emission, which can then be measured instrumentally if needed.

Some chemical sensing materials utilize changes in current or resistance measured to register the presence of a pollutant. In theory the response of the sensor could be calibrated for a specific chemical or group of chemicals. A broad range of compounds could be detected via this type of sensor, but wide-range detection is rare for any single sensor. Sensor composition is dependent upon its intended application. Electronic signal-based sensor materials can take a variety of forms, including solid or liquid electrolyte, ion selective electrodes, and piezoelectric electrodes. For the most part these sensors are used to quantify and detect simpler analytes such

as atomic or ionic species. Examples include ion, pH, and oxygen sensing.[5,6] An additional obstacle is that the sensor must be carefully calibrated to create a system of quantitative responses to specific compounds. Miscalibrated sensors can lead to problems in correctly quantifying the analytes. A further obstacle is that some technology is needed to measure and evaluate the current change. In some cases it would be more effective if a visual analysis could be used to evaluate the presence of analyte.

An alternative possibility for a sensor that can be used either visually or instrumentally is one based on color change or light emission change. Emission-based detectors are quite promising for detection of organic pollutant molecules. Emission in this context is a physiochemical process by which an atom, molecule, or ion emits light. The process begins with absorption of light of the correct energy to promote an electron to a higher energy state. When this electron decays back to the former ground state, it emits light (a photon) corresponding to the energy difference between the ground state and the excited state. Although one might expect the emission energy to be exactly the same as that absorbed, this is not always, or even usually, the case. Atomic transitions can be observed at exactly the same absorption and emission energies, but the occurrence of vibrational states in molecules and complexes results in broader emission band width than seen in atomic or ionic spectra. An overview of the process of absorption and emission is shown in the Jablonski diagram in Figure 1.4. Luminescence is the radiative recombination of an excited electron and the hole paired with it to produce a photon. There are other pathways for relaxation for an excited electron.

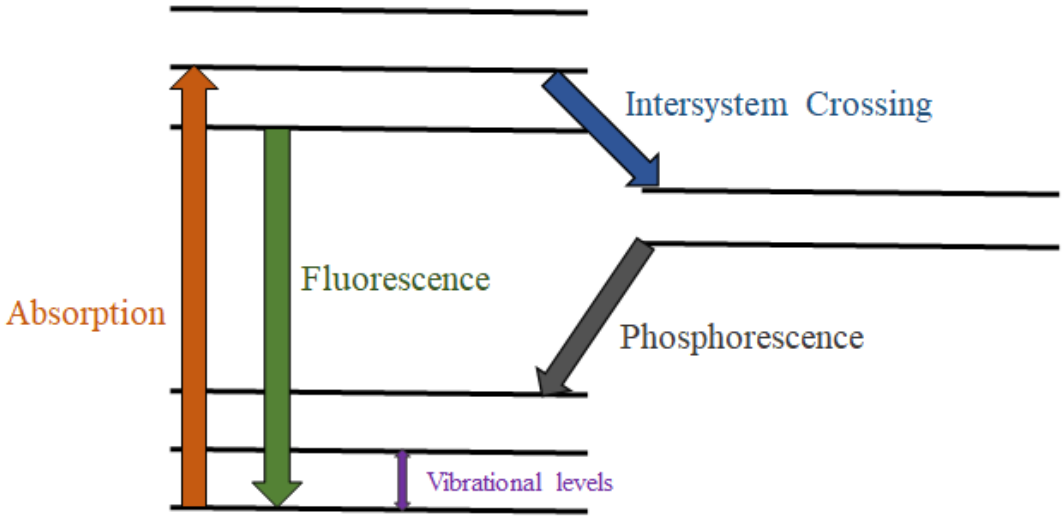

Figure 1.4: A Jablonski diagram showing the processes of absorption, fluorescence, intersystem crossing, and phosphorescence.

Contributing factors are vibronic energy levels, non-radiative decay (relaxation by heat), and inter-system crossing which can lead to shifts in the energy of emission. Generally the shift is to lower energies and is often referred to as a Stokes shift. As shown in Figure 1.4, once light has been absorbed the electron can quickly return to the ground state and release a photon. This photon energy can be lower if the excited electron relaxed through one or more vibrational states before making the return to its original energy. Another option is the excited electron can undergo intersystem crossing, where a spin conversion can take place. The spin conversion/intersystem crossing pathway takes significantly longer than an emissive recombination via luminescence. The longer time frame associated with intersystem crossing and phosphorescence can facilitate more alternative thermal relaxation. If this process is repeated, essentially all of the excited electrons energy can be bled off in the form of thermal relaxation. So with sufficient vibrational energy states available, a molecule or complex can absorb a photon of a given energy but display no emission characteristics. A sensor that can transition from an emissive state to a non-emissive

state or vice versa would be ideal for a chemical sensor based on luminescence. An example of how a luminescence based chemical sensor would operate can be seen above in Figure 1.3.

There are several potential advantages to a sensor that provides a measureable response via a change in emission color and/or intensity. Luminescence in general is an extremely sensitive technique that provides excellent limits of detection (LOD). One of the limiting factors for high sensitivity and LOD is confounding influences in the sample matrix. The background emission for water and air is non-existent in the visible and near UV, so the potential for LOD is usually extremely low in these matrices. Alternatively, if multiple species that produce signal in the same spectral range are present, differentiating between them can be challenging and sensitivity suffers. For emissive organic molecules, emission normally occurs in the high energy region of the visible or into the UV. A sensor that primarily responds outside of this range could avoid this interference. Moving the response further into the visible has the added bonus that the response can be evaluated visually as a colorimetric sensor. Furthermore, the minimum electrical equipment that would be required to test the emission would be a portable UV light, which is relatively inexpensive and readily available. The ready availability of portable UV lights means an emission-based sensor could be brought on site and visually inspected upon exposure to the sample. This would allow for rapid collection of qualitative results. Two applications for a qualitative colorimetric sensor would be as a warning device that toxic chemicals are in the environment, or as a screening test to reduce the number of samples that need to be run instrumentally. As an added advantage, the sensor could be incorporated as part of a more sophisticated detector that reads the wavelength. It could be possible to correlate specific wavelengths to certain compounds or classes of compounds for more detailed analysis. The large breadth of molecular emission bands could present an obstacle to the detailed analysis of these compounds, so there are still challenges to be met with detection for these materials.

In order to construct a luminescence sensor the sensing material could be fabricated as a surface, used in powder form, or even used in solution, depending on solubility. The simplicity of this type of sensor is attractive, but the performance characteristics must be up to par. As mentioned above, luminescence offers potentially excellent sensitivity and LOD. Additionally, tuning of the detector to a specific wavelength would help to specifically identify compounds of interest.

Most chemical sensing materials that have been investigated to date have often been composed at least partially of metals or metal compounds.[7-13] The metal species function in two ways. First, the metal centers often serve as coordination points for the incoming analyte. This works well for organic analytes that typically have nucleophilic groups present that can interact with the normally electrophilic metal center. Another role served by the metal is in producing the emission, which is often based on a ligand to metal charge transfer (LMCT) process. Thus, metals are quite promising for use in these types of chemical sensing applications. However, often the metals considered in detector applications, e.g. platinum, are expensive and as a result impractical for use in larger scale, or in disposable sensors. Instead, it may be necessary to find metal-based sensor materials that are much more practical for use in sensing applications.

One metal with both promising chemical properties and low cost is copper[14-19]. Copper-based chemical sensors have a number of potential advantages stemming from the chemical versatility of copper, low cost, and negligible toxicity. Copper is most commonly found in the +1 and +2 oxidation states. Under normal circumstances, only Cu(I) produces visible luminescence emission. Copper(I) is a fairly soft metal ion and so favors soft binding partners. This softness is potentially quite useful since OP can contain soft nucleophilic groups such as sulfur and nitrogen. These soft nucleophiles pair favorably with copper(I).[20,21] Examples of simple copper(I) salts are CuCl, CuBr, CuI, CuCN, and CuSCN. Of particular focus here is copper(I) iodide (CuI) complexes.

CuI has three known crystal structures depending on the temperature. For the purposes of a chemical sensor, only the γ-CuI form is relevant. It is the only form observed at room temperature. The structure of γ-CuI is shown below in Figure 1.5.

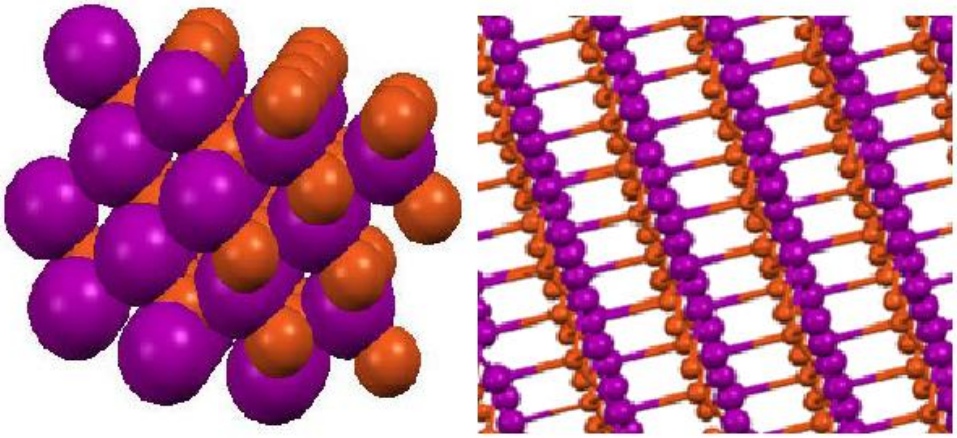

Figure 1.5: γ-CuI in space filling form (left) and in ball and stick (right). Copper atoms are orange, iodine are purple.

At room temperature CuI is a beige powder that displays faint pink or purple emission under UV irradiation. It is shelf stable and much more resistant to oxidation than other copper halides. The +1 charge on the copper lends itself to soft Lewis acid reactivity. Coordinating ligands with atoms such as nitrogen and sulfur find very high affinity with the copper center in CuI. The muted reactivity of CuI with harder nucleophilic species (such as those involving oxygen atoms) somewhat limits the range of complexes that can be formed, but this reduced oxophilicity certainly improves the stability of CuI toward oxidation. The zinc blend structure (γ-CuI) is stable at ambient temperature and up to 390 ^{o}C. CuI can form complexes with ligands to create a number of different structures beyond those shown above.

Understanding the morphology of Cu(I) complexes is critical for explaining its chemical properties. These different structural forms can have an effect on both the traditional reactivity and the emission behavior of the material. Four common structures are shown below in Figure 1.6.

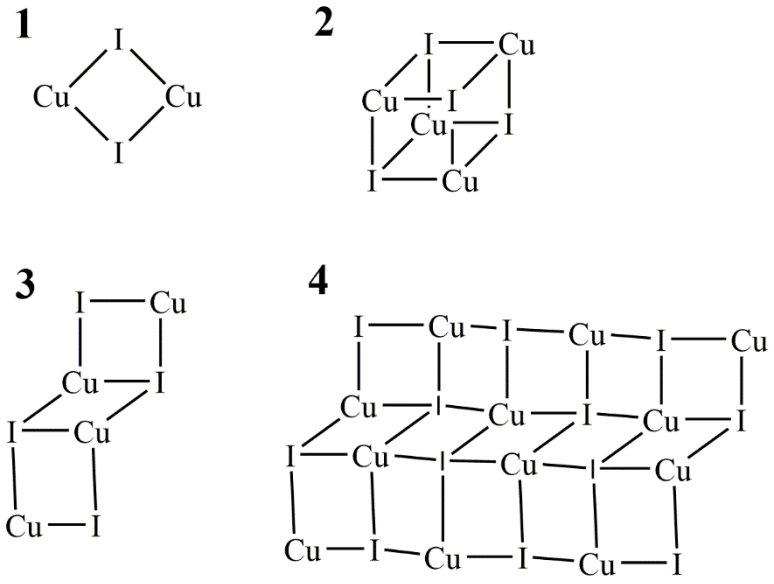

Figure 1.6: Morphologies of CuI compounds: dimer (**1**), cubane (**2**), ladder (**3**) and sheets (**4**).

The coordination flexibility of Cu(I) in CuI complexes means coordination by ligands can occur at the copper sites that have coordination numbers >4. For some of the lower coordination number units such as the dimer, Cu could potentially coordinate two ligands. Furthermore, some specific emissive behavior can be attributed to specific structural types. A well-known example is the presence of a cluster centered transition in the cubane Cu_4I_4 (**2**).[22] At low temperatures a new lower energy transition was observed that was attributed to an internal cluster transition between the halide and the metal[22] (XMCT). Thus the structure has great importance for predicting and explaining the luminescent behavior of CuI compounds.

Although normally found as white or off-white powders, many Cu(I) compounds display emission in the visible range arising from the charge transfer capabilities between the copper

center and the ligands in the complex. There is significant literature showing the production of CuI complexes with varying emission colors under UV irradiation.[23] Visible emission colors are often in the yellow to red range, although higher energy emission also occurs.[23] The wide range of CuI emission colors upon reaction with various nucleophiles, as demonstrated in our group's previous research is shown below in Figure 1.7.

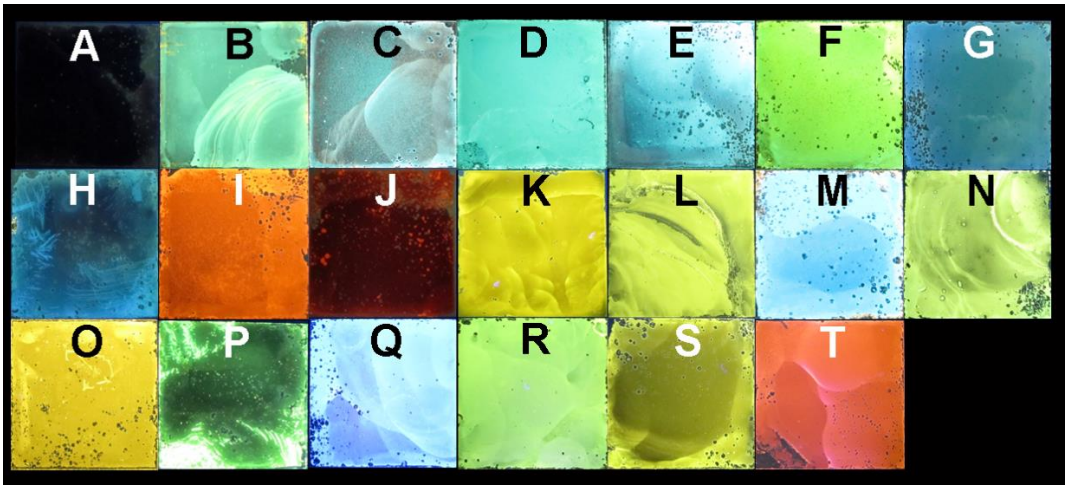

Figure 7: Shown are images of CuI complexes with varying amines and sulfides.[23]

The range of colors observed in the CuI(L) complexes is demonstrative of the operative emission mechanisms. There are two commonly described emission pathways for these complexes. One is a cluster-centered transition that is typically operative at room temperature and is seen in the visible range.[22] When the compound is cooled to low temperatures, a higher energy band that is often absent at ambient temperature is evidenced at shorter wavelengths. This band corresponds to a halide to ligand charge transfer (XLCT). This behavior can be further complicated by the involvement and mixing of metal orbitals to produce metal to ligand charge transfer (MLCT) and mixed halide/ligand to metal charge transfer. The relative energies of the ligand orbitals and the orbitals associated with the particular $(CuI)_x$ cluster can have a significant effect on the emission energies observed. Therefore, even structurally similar ligands can produce

quite different emission colors.[23] This type of emission behavior is a natural fit for a selective detector.

Although there is extensive literature on the complexation of CuI with ligands to create emissive products, studies on the use of CuI as a chemical sensor are vastly more limited. Figure 1.7 shows preliminary evidence for a degree of selectivity associated with CuI as a chemical sensor.[23]

One of the major considerations of an effective chemical sensor is the speed of its response. Our previous work on CuI has shown that although CuI reacts readily with ligands like pyridine and dimethyl sulfide, the reaction can be quite slow with reaction times as long as minutes[23,26]. To be an effective chemical sensor the reaction of CuI with the incoming nucleophile should take place over seconds, not minutes. Improvement on the rate of reaction for this system must be investigated. Additionally, although the reaction of CuI with nucleophiles has been demonstrated in the vapor phase and in the solid state as a possible foundation for a chemical sensor, the viability of this reaction in water has not yet been addressed. These questions of reaction rate and aqueous sensing are addressed in this thesis.

2) **Experimental and Instrumentation**

Materials:

All reagents were purchased from Aldritch or Acros and used without further purification.

Instrumentation:

Single Crystal X-Ray Diffraction:

Single crystals were mounted on glass fibers and data was collected at 100 K. Measurements were made on a graphite monochromated Mo source with Kα radiation or a Cu microfocus source using Kα radiation. These measurements were made on a Bruker DUO three circle diffractometer outfitted with an APEX II detector. Initial space group determination was done with a matrix run of 36 and 90 runs for Mo and Cu respectively. Data was corrected for Lorentz an polarization effects and absorption using SADABS[24]. All structures were solved using intrinsic phasing and refined using SHELXTL[25] and ShelXle. All non-hydrogen atoms were refined anisotropically and hydrogens were placed at theoretical positions. Where necessary the twin correction function of the SHELXTL software was used to solve structures.

Powder X-Ray Diffraction:

Powder patterns were collected on an Thermo Scientific Equinox 100 benchtop X-Ray diffractometer. Samples were ground and placed into the sampling cup without further modification. Data was collected using a Co microfocus Kα source and the EQUINOX curved gas cell detector. Data was collected simultaneously across the range of 10-70 2θ for 300 seconds/scan. Data was exported from the instrument computer in xy format where it could be converted using Bragg's Law to the shifts expected for Cu Kα radiation for consistency with predicted patterns from the single crystal measurements. All calculated powder patterns were created with the use of the calculate function in the Mercury program.

Thermogravimetric Analysis:

Thermogravimetric Analysis (TGA) was conducted on a TA instruments Q500 at the dynamic variable heating rate. The runs were completed with a maximum heating rate of 50 ^{o}C/min to 800 ^{o}C with a flow rate at either 40 or 50 mL of N_2/min.

Fluorimeter Measurements:

Fluorimeter measurements were collected on a Perkin-Elmer LS-55 spectrofluorimeter. Both the solid module and the liquid sample module were used depending on required measurements. The voltage of the photomultiplier was altered to increase the signal without oversaturating the detector. A stir motor was modified to allow stirring of suspension samples in the liquid sample holder during sample collection. The scans were taken in replicate and averaged.

Atomic Absorption:

Copper and silver content were quantified using a Perkin-Elmer AAnalyst 700 instrument. For copper analysis alone the samples were dissolved in nitric acid, then diluted first to 100 mL and then to 25 mL. For the nanoparticles specifically, each sample was dissolved in 1.5 M KI and then again in H_2O to approximately 4 mg/L. Each sample was measured 3 times and the average of the values was reported.

Transmission Electron Microscopy (TEM):

TEM data was collected at the University of Maine Electron Microscopy Laboratory. The Phillips/FEI CM 10 TEM was operated at specifications of 0.5 nm point resolution and 0.3 nm lattice resolution. The magnification ranged from 25x to 450,000x with an accelerating potential of 100 kV. Nanoparticles were deposited from solution onto copper grids coated in amorphous carbon. A single drop of the nanoparticle solution was deposited via pipette and allowed to dry at room temperature.

Solid State Luminescence:

Solid state luminescence data was collected at the University of Maine with a Model Quantamaster 1046 photoluminescence spectrophotometer from Photon Technology equipped with a 75 W xenon arc lamp and 2 excitation monochromators and one emission monochromator. A photomultiplier tube detector was used at 800V. The samples were placed on a copper plat using non emitting copper dust high vacuum grease.

Kinetics Measurements:

A custom built system at the University of Maine was used to measure kinetic data. The system was built to expose a solid sample to a fixed concentration of gas using flooding conditions, and then measure the emission output. A sample of 2 mg of the nanoparticles was placed on a glass slide and then exposed to a mixed gas with a known amount of VOC. This was accomplished by bubbling air through liquid dimethyl sulfide (DMS) at ambient temperature and then mixing that gas at a 1:1 ratio with air. This final mixture was the gaseous one the nanoparticles would be exposed to. The gas flow rate was either set to 43.3 μmol hr^{-1} or 86.7 μmol hr^{-1}. The system was purged for 5 minutes to ensure even concentration, and then the valve was closed and the nanoparticles were moved into position directly under the output of the gas. During evaluation a 350 nm mercury lamp was used as an excitation source and a fiber optic cable for collection of light. An Ocean Optics spectrophotometer was used as the detector for the outgoing light. A scan was taken in the dark to be used as a blank. Each sample was measured until no further change in emission was observed. Each trial was conducted three times and averaged.

Molecular Dynamics:

Molecular dynamics simulations were performed by David Welch of Suffolk County Community College. The calculations were done in the NANIM simulation program[25] and the NVT ensemble with 2 fs time steps, an equilibration of 100 ps, and production time of 100 ps. The temperature was set to 298 K using the velocity rescaling thermostat of coefficient 0.01 ps)[26]. The simulations were performed four times each and the statistical results averaged.

SYNTHESIS:

CuAgI Nanoparticles:

For the synthesis of CuI nanoparticles, CuI (0.800 mmol) was added to 20 mL of 3 M KI. While stirring aggressively 5 mL of ethanol and 15 mL acetonitrile were added. While continuing the high stir rate, water was added at a rate of 1 drop every 5 seconds. An off white powder gradually crashed out of solution and was isolated with centrifugation. The samples were washed twice with water and once with ethanol. For the other two ratios, the above was followed except the desired molar ratio was reflected in the ratio of CuI to AgI used. The silver containing nanoparticles were markedly more yellow in color than the pure CuI.

CuI/2-PyCN Evaporation Experiment

A solution containing 2-PyCN (162 mg, 1.6 mmol) in 20 mL MeCN was added to a CuI solution (324 mg, 1.7 mmol) in 5 mL MeCN. The yellow solution produced was reduced to 20 mL in volume and then filtered. This solution was transferred into an uncapped 2 dram vial at room temperature in a fume hood.

The solution was allowed to evaporate to about half of the original volume and the liquid was pipetted out of the vial and into a new one. The solid that has manifested on the walls of the vial was examined. The highest band was yellow-orange in color and weakly orange emissive. Closer examination under a microscope revealed hexagonal plate crystals. The structure of the hexagonal plates was solved as $(CuI)_2(2\text{-}PyCN)_4$(**1**). The next band of solid contained yellow needles. Under UV light a minor portion was non-emissive and a larger portion was green emissive. The green emissive areas corresponded to small yellow needles that tended to grow in starburst patterns. The structure of these needles was solved as $(CuI)_3(2\text{-}PyCN)$(**3**). The non-emissive yellow needles tended to be larger and did not cluster. The structure of the non-emissive needles was solved as CuI(2-PyCN)(**2**). Further evaporation led to primarily the green

emissive **3**. When evaporated to dryness, the solid at the bottom of the vial was a mottled mixture of **3** and what appeared to be CuI.

$(CuI)_2(2\text{-PyCN})_4$, (**1**)

2-PyCN (1001 mg, 9.62 mmol) was melted with gentle heating in a capped vial. CuI (190 mg, 1.00 mmol) was added to the melt and the headspace was flushed with argon. The mixture was stirred for 48 h at 60 °C in a thermostatic oil bath. The suspended yellow powder was collected via filtration, washed with ethyl ether, and dried under vacuum (310 mg, 0.389 mmol, 77.8%). The yellow product emitted yellow-orange under 365 nm. IR (cm^{-1}): 3055, 2237 (CN), 1585, 1466, 1435, 1292, 1292, 1207, 1157, 1096, 1007, 910, 764 (strong), 640. Anal. Calcd for $C_{24}H_{16}Cu_2I_2N_8$: C, 36.15; H, 2.02; N, 14.05. Found: C, 35.46; H, 1.85; N, 13.63. TGA Calcd for $(CuI)_3(2\text{-PyCN})$: 56.5%. Found: 58.2% (65–110 °C). Calcd for CuI: 47.8%. Found: 49.7% (110–180 °C).

$(CuI)_3(2\text{-PyCN})$, (**3**)

CuI (381 mg, 2.00 mmol) was dissolved in 20 mL of MeCN, and 2-PyCN (210 mg, 2.02 mmol) was dissolved in 5 mL of MeCN in a separate vessel. The 2-PyCN solution was added dropwise to the solution of CuI at 0 °C with stirring. The resulting brown solution was concentrated to 20 mL under reduced pressure at room temperature. A finely divided black solid gradually accumulated at the bottom of the flask and the liquid displayed a gray-green color. The black solid was filtered leaving a yellow solution, which was placed in a −8 °C freezer overnight. The yellow needle crystals were filtered and washed with ethyl ether. The mother liquor concentrated to approximately half its volume, and the process repeated three times. The yellow needle crops were combined and dried under vacuum (270 mg, 0.400 mmol, yield = 60.0%). The product emitted green under 365 nm irradiation. IR (cm^{-1}): 3071, 2245 (CN), 1682, 1582, 1458, 1427, 1284, 1207, 153, 1092, 1049, 1006, 907, 764 (strong). Anal. Calcd for $C_6H_4Cu_3I_3N_2$: C, 10.67; H, 0.60; N, 4.15. Found: C, 10.87; H, 0.50; N, 4.05. TGA Calcd for CuI: 84.6%. Found: 85.1% (145–175 °C).

$(CuI)_2(3\text{-}PyCN)_4$, (4)

CuI (195 mg, 1.02 mmol) was dissolved in 10 mL of MeCN and 3-PyCN (494 mg, 4.75 mmol) was dissolved in 5 mL of MeCN in a separate vessel. The CuI solution was added dropwise to the solution of 3-PyCN with stirring. Upon addition of the CuI solution, a light-yellow product immediately precipitated. The resulting product was filtered, then washed with MeCN and dried under vacuum (254 mg, 0.319 mmol, 62.5%). The yellow-green product emitted intensely green under 365 nm irradiation. IR (cm^{-1}): 3055, 2237 (CN), 1589, 1466, 1435, 1292, 1207, 1157, 1096, 1049, 1007, 910, 764 (strong), 640. Anal. Calcd for $C_{24}H_{16}Cu_2I_2N_8$: C, 36.15; H, 2.02; N, 14.05. Found: C, 36.30; H, 1.93; N, 13.85. TGA Calcd for (CuI)(3-PyCN): 73.9%. Found: 69.4% (120–125 °C). Calcd for CuI: 47.8%. Found: 48.7% (95–150 °C).

(CuI)(3-PyCN), **(5)**

CuI (152 mg, 0.798 mmol) was dissolved in 5 mL of MeCN and 3-PyCN (82.0 mg, 0.788 mmol) was dissolved in 10 mL of MeCN in a separate vessel. The 3-PyCN solution was rapidly added to the solution of CuI with stirring. A yellow solution formed and was immediately covered and placed in a −8 °C freezer. Yellow needles formed overnight. This product was filtered, and a second crop was produced similarly after concentrating the mother liquor to half its volume. The combined crops were washed with ethyl ether and dried under vacuum. (164 mg, 0.557 mmol, 69.8%). The yellow-orange product emitted yellow under 365 nm irradiation. IR (cm^{-1}): 3067, 2234 (CN), 1589, 1466, 1416, 1188, 1030, 810 (strong), 675 (strong), 644. Anal. Calcd for $C_6H_4CuIN_2$: C, 24.47; H, 1.37; N, 9.51. Found: C, 24.53; H, 1.29 N, 9.42. TGA calcd for CuI: 64.6%. Found: 65.2% (110–150 °C).

$(CuI)_4(4\text{-}PyCN)_5$, (6)

CuI (315 mg, 1.65 mmol) was dissolved in 5 mL of 5 M aq. KI solution and 4-PyCN (199 mg, 1.91 mmol) was dissolved in 5 mL of 5 M aq. KI solution in a separate vessel. Under stirring, the 4-PyCN solution was added slowly to the solution of CuI, immediately producing an orange precipitate. The product was filtered, then washed with 5 M aq. KI solution, water, 95% ethanol,

then ethyl ether and vacuum dried (347 mg, 0.271 mmol, 65.6%). The orange product emitted orange under 365 nm irradiation. IR (cm^{-1}): 3032, 2241 (CN), 1597, 1539, 1489, 1412 (strong), 1215, 1068, 1007, 826 (strong), 783. 671. Anal. Calcd for $C_{30}H_{20}Cu_4I_4N_{10}$: C, 28.10; H, 1.57; N, 10.92. Found: C, 27.89; H, 1.46; N, 10.68. TGA Calcd for CuI: 59.4%. Found: 61.1% (115–160 °C).

$(CuI)_4(3\text{-}PyNO_2)_4$, (7)

CuI (1001 mg, 5.26 mmol) was dissolved in 40 mL of MeCN. To this solution with stirring was added solid 3-$PyNO_2$ (651 mg, 5.25 mmol), causing the solution color to change from yellow to orange. The solution was concentrated to 10 mL under vacuum and then cooled to −8 °C overnight. The orange block crystals that formed were isolated by decanting. The mother liquor volume was reduced by half and cooled to −8 °C again, producing a second product crop. The combined crops were washed twice with ethyl ether and dried under vacuum (1123 mg, 0.893 mmol, 68.0%). The orange crystalline product was non-emissive under 365 nm irradiation. IR (cm^{-1}): 3075, 1612, 1527 (strong), 1435, 1350 (strong), 1192, 1107, 1030, 856, 822, 725, 714, 678 (strong). Anal. Calcd for $C_{20}H_{16}Cu_4I_4N_8O_8$: C, 19.09; H, 1.28; N, 8.91. Found: C, 19.12; H, 1.08; N, 8.72. TGA Calcd for CuI: 60.5%. Found: 61.8% (100–145 °C).

$(CuI)(3\text{-}PyNO_2)$, (8)

CuI (512 mg, 2.69 mmol) was added to 10 mL of MeCN to create a partial solution. To this mixture with stirring was added solid 3-$PyNO_2$ (321 mg, 2.59 mmol). The resulting suspension was refluxed overnight under Ar, producing a red-orange solution. The solution was hot-filtered and cooled in an ice water bath. Red blades were collected by filtration (412 mg, 1.31 mmol, 50.6%). Note: This reaction can sometimes produce the orange polymorph (**7**). To help alleviate this problem the solution can be seeded with a red crystal. The red crystalline product was non-emissive under 365 nm irradiation. IR (cm^{-1}): 3094, 1609, 1520 (strong), 1431, 1350 (strong), 1192, 1103, 1030, 856, 826, 725, 710, 679 (strong), 632. Anal. Calcd for $C_5H_4CuIN_2O_2$: C, 19.09;

H, 1.28; N, 8.91. Found: C, 19.24; H, 1.10; N, 8.95. TGA Calcd for CuI: 60.5%. Found: 60.6% (125–160 °C).

3) A Mechanistic Investigation of CuAgI Heterometallic Nanoparticles as Sensors for Gas Phase DMS:

Copper(I) and its d^{10} congeners are a continuing source of interest in recent years. The complexes and networks formed from these ions can exhibit luminescence stemming from the inter-network interactions taking place. Furthermore, the emission can be tuned to varying degrees by altering the ligands that are used. One of the potential uses for these complexes is the interaction of a metal-based substrate with a volatile organic compound (VOC). The reaction occurs at the interface between the material and gaseous VOC to produce a change in color and/or emission. This phenomenon is called vapochromism. One of the challenges to research in this area is that the effects of vapochromism are well documented but the mechanism of action is poorly understood. An example of vapochromism in work previously published by the Pike group is shown below in Scheme 1.

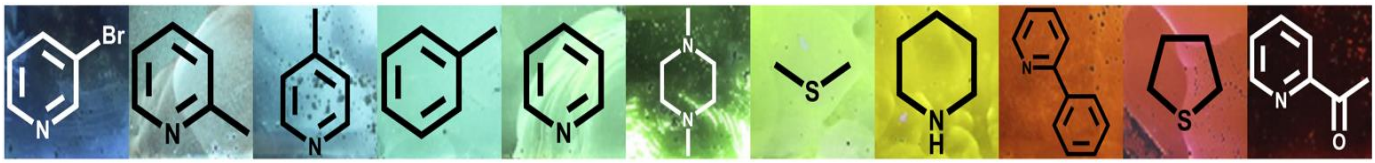

Scheme 1. Visible light photos of previously reported CuI films from our group under 365 nm irradiation after exposure to various VOC vapors.[27]

Scheme 1 shows the variety of photoemission colors as a result of VOC interaction with a solid substrate of CuI. While there is some promising evidence for selectivity, with the different colors associated with different ligands, the rate of reaction with a gaseous nucleophile leaves something to be desired. To increase the reaction rate, we moved to working with mixed metal

systems. This direction was inspired by the work of Danny Leznoff *et al.* on coordination polymers based on mixed Cu/Ag cyano composition. His observation was that the ratio of the heterometallic systems can be tuned to optimize the vapochromic reactivity of the substrate.[28,29] Although his findings are practically useful, the mechanism of action for this behavior is currently poorly understood. It is further complicated by X-ray studies by Leznoff *et al.*, which indicate that the ligand binding occurs exclusively at copper sites[28,29]. Further understanding of the mechanism at work will certainly help produce improvements in the vapochromic sensor field and contribute to general chemical knowledge.

It was with this goal in mind that the Pike group set out to conduct a mechanistic study of the reaction between group 10 metal iodides with dimethyl sulfide (DMS) in collaboration with the Patterson group at the University of Maine and Dave Welch of Suffolk County Community College. The work proceeded with a two pronged approach of using both experimental and computational studies to elucidate the heterogeneous reaction behavior of this system. The target substrate material for this study was CuI nanoparticles synthesized with varying ratios with Ag to produce $Cu_xAg_{1-x}I$ nanoparticles (NP). Nanoparticles were chosen for their high surface area with an eye to increasing reaction rates through improved substrate exposure to DMS.

The NPs were synthesized by a co-precipitation technique in a water/acetonitrile/ethanol mixture to produce CuI (**1**), $Cu_{0.75}Ag_{0.25}I$ (**2**) and $Cu_{0.50}Ag_{0.50}I$ (**3**). The metal composition ratios of the NP samples were confirmed using atomic absorbance spectroscopy (AAS) with good agreement with theoretical values. Powder X-ray diffraction (PXRD) was conducted on the three NP samples. The results are shown below in Figure 3.1.

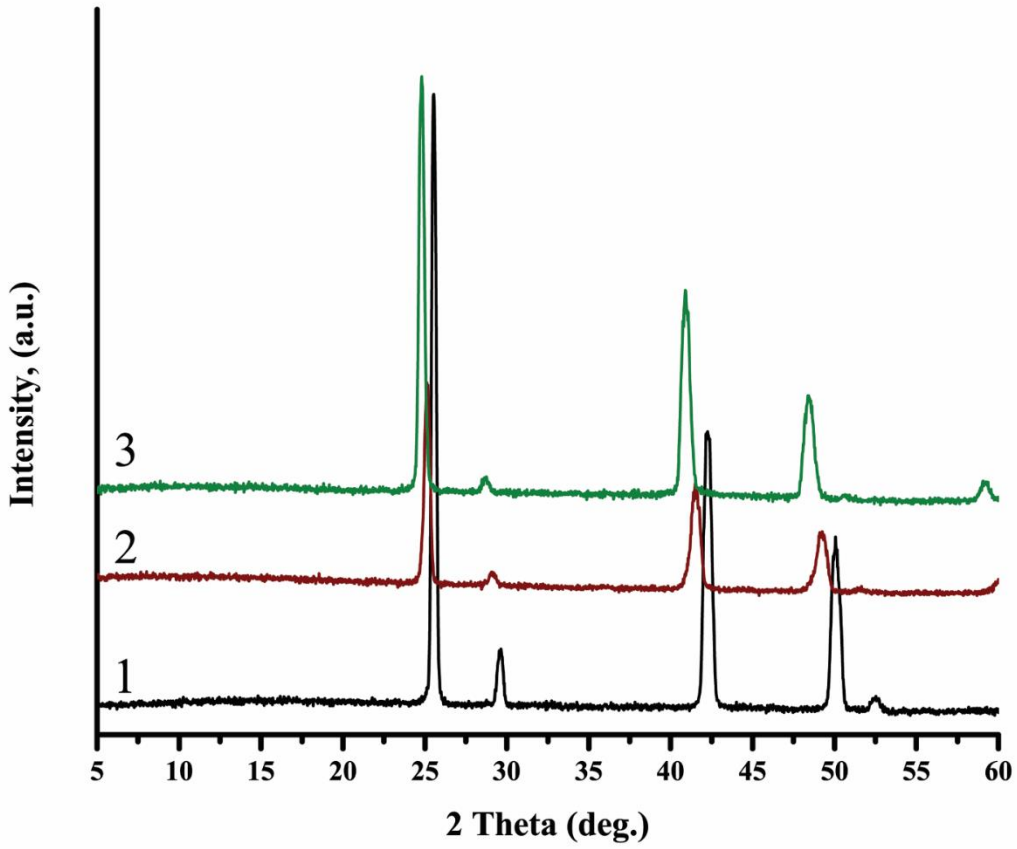

Figure 3.1: PXRD traces of **1**, **2**, and **3**.

PXRD shows a common pattern for **1** that matches the zinc blende pattern for γ-CuI. The silver-containing samples **2** and **3** showing similar patterns but with increased lattice parameter, resulting in slight peak shifting with increasing silver content. To confirm that the products of the synthesis are NPs, transmission electron microscopy was completed on samples of **1**, **2**, and **3**. The results are shown below in Figure 3.1. The TEM analysis showed a range of variation in size, but the particles were found to be within the nanometer size range.

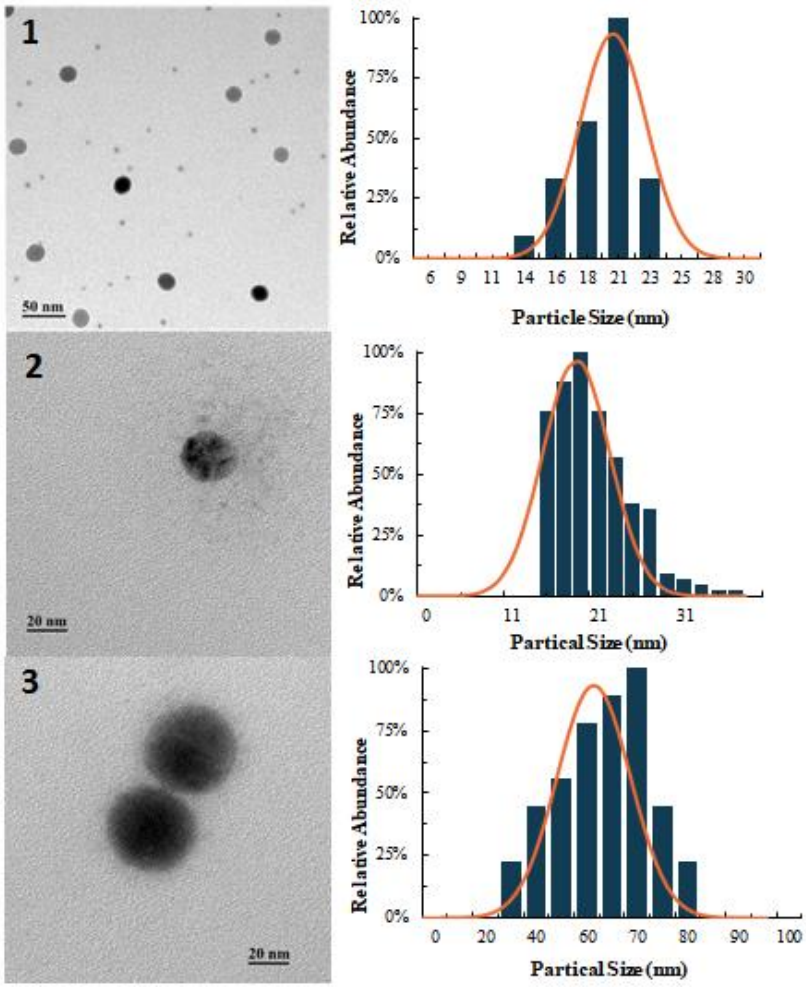

Figure 3.2: TEM images of **1**, **2**, and **3** (left) and a size distribution analysis (right).

When exposed to UV light, NP samples **1** and **2** show emission, while **3** does not. The emission observed for **1** and **2** matches previously observed emission for CuI that likely stems from an internal charge transfer between I^- and Cu^+.[30,31] By incorporating increasing amounts of silver ion, this interaction is disrupted and so mitigates some of the emissive properties. The NP samples were exposed to DMS vapor. A reaction was observed in all three cases, producing the CuI-DMS complexes **1′**, **2′**, and **3′**. The DMS-exposed samples underwent a change in their photoluminescence behavior, transitioning from the pink emission of CuI to green-yellow

emission that was indicative of the CuI-DMS complexes. This behavior is illustrated below in Figure 3.3.

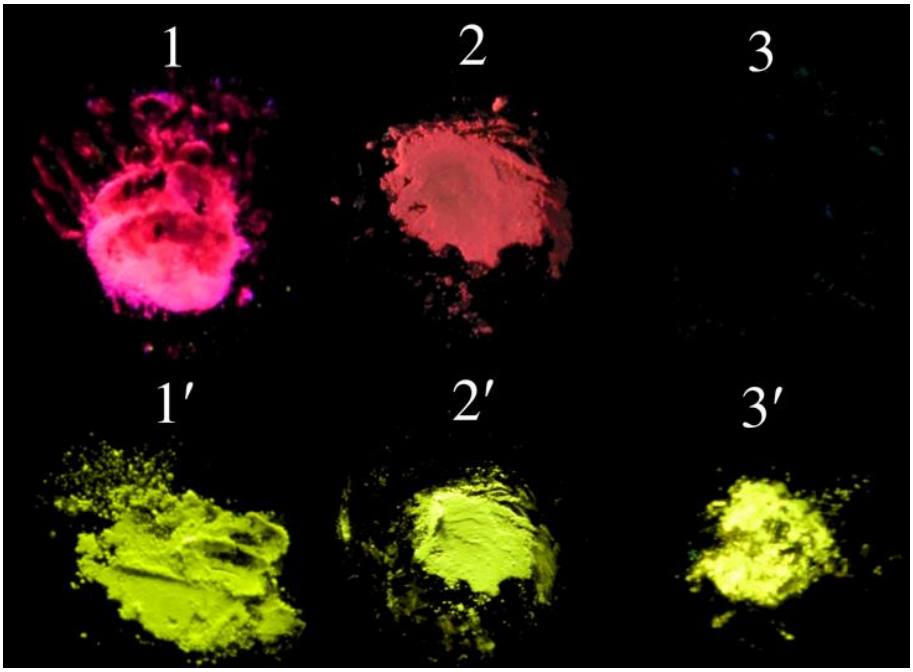

Figure 3.3: Samples before (top) and after (bottom) DMS exposure under 365 nm irradiation.

Thermogravimetric analysis (TGA) was carried out on the exposed samples and then repeated on the samples following vacuum treatment overnight. The results are shown in Figure 3.4. The TGA traces for **1′**, **2′**, and **3′** show the loss of DMS consistently at 70-80 ^{0}C. The TGA data give insight into how much DMS was picked up by each sample. The mass percent of DMS was 18.2%, 5.5%, and 8.2% for **1′**, **2′**, and **3′** respectively. Sample **1′** picked up significantly more DMS than the heterometallic compounds.

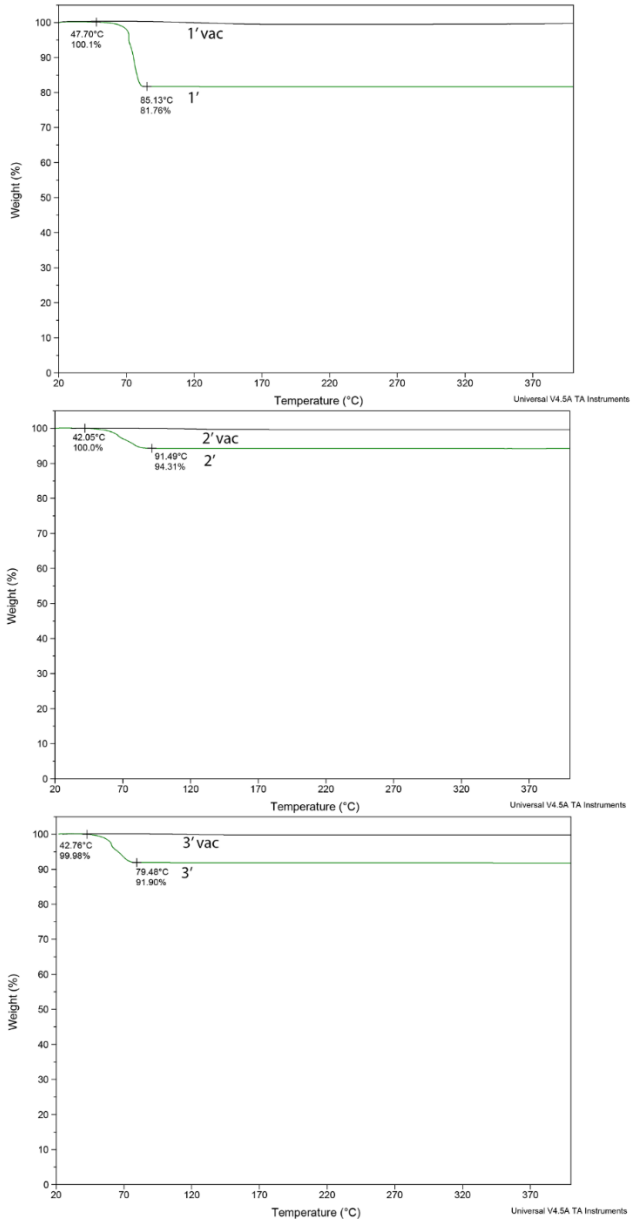

Figure 3.4: TGA of DMS-exposed samples **1′**, **2′**, and **3′** before and after vacuum treatment.

PXRD was conducted on the exposed samples **1′**, **2′**, and **3′**. The PXRD is shown in Figure 3.5 with a calculated pattern for $(CuI)_4(DMS)_3$. The powder XRD is largely a surface analysis technique. The data collected shows that as the silver content increases, there is an evolution of a peak indicating increasing Cu/AgI character. As that increase occurs, and given that silver is a bystander in this reaction, the increased inclusion of silver decreases the amount of DMS that can be coordinated. In this way the PXRD is supportive of the TGA findings.

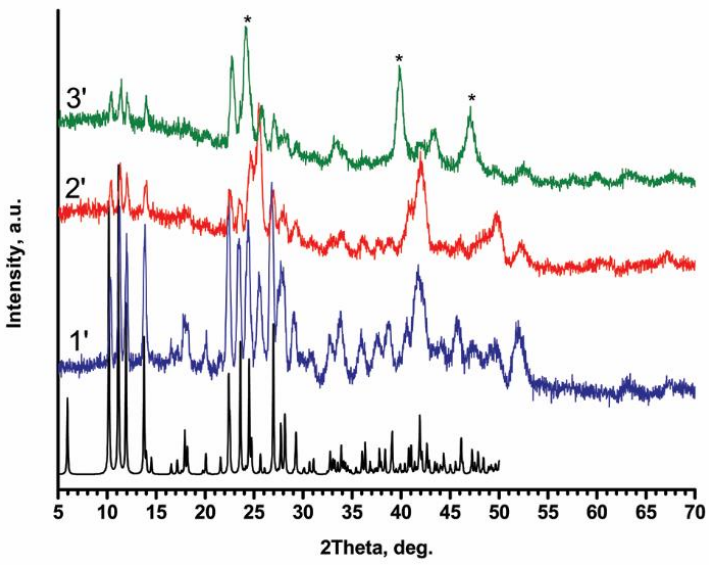

Figure 3.5: PXRD traces of **1′**, **2′**, and **3′** and calculated PXRD pattern for $(CuI)_4(DMS)_3$ (black). The asterisks indicate peaks due to CuI/AgI.

Turning now to the luminescence emission spectroscopy of the DMS-exposed NPs, samples **1′**, **2′**, and **3′** were each emissive (see Figure 3.2, above), however the emission intensity was seen to decrease as the silver content increased. Each sample displays matching emission at 550 nm, as shown in Figure 3.6. All three exposed samples emit the green-yellow color that matches the emission profile previously reported for $(CuI)_4(DMS)_3$[27].

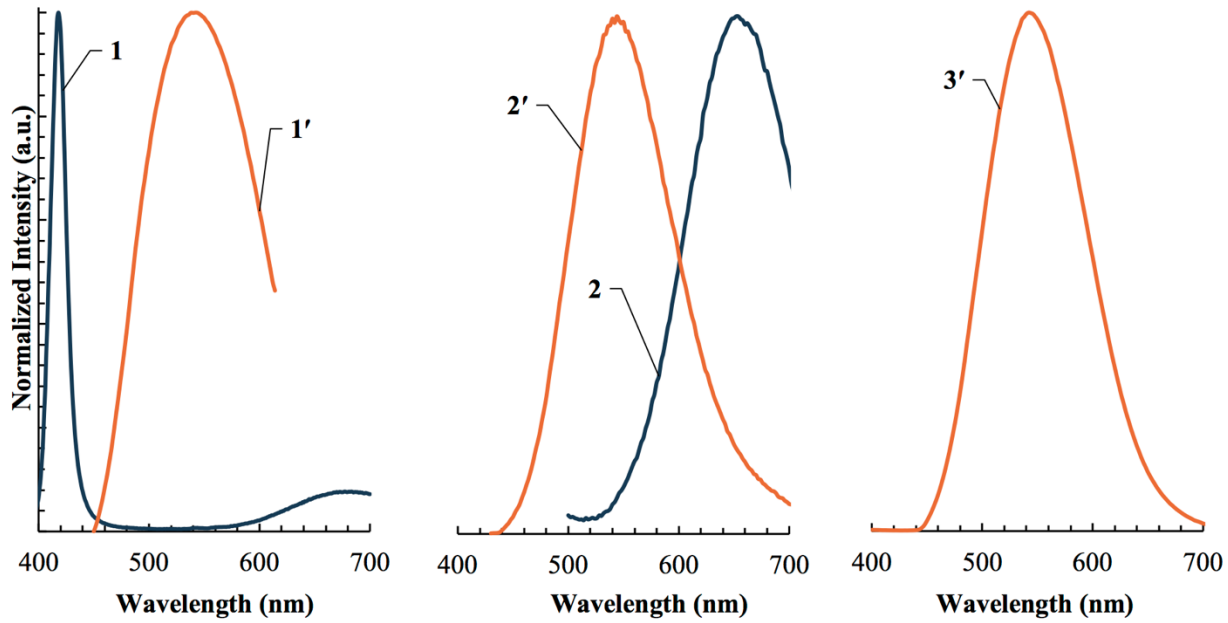

Figure 3.6: Solid state luminescence emission profiles for NP samples **1**, **2**, and **3**, and exposed samples **1′**, **2′**, and **3′**. There is no observed emission for **3′**.

Taken together, the experimental data support the idea that the final product is the previously reported $CuI_4(DMS)_3$ based on the emission profile[27]. Furthermore, the increased presence of silver reduces the amount of DMS that can coordinate to the CuAgI sample. As an additional technique to probe the system being studied, molecular dynamics calculations were undertaken. The solid substrate was modeled as block of crystalline copper iodide with the 111 surface exposed and with cation terminations. Silver was doped in for Cu in varying amounts to simulate the heterometallic materials made experimentally. The mechanics model revealed that the affinity for DMS was higher for silver sites than for copper sites by 1.2 kJ/mol. The implication is that the DMS molecules will more readily adsorb to a surface that features at least some silver, whereby the binding affinity is greater. This is an unexpected finding insofar as the experimental data showed less complete reaction in the samples that contained silver. Nevertheless explanation comes from the fact that it is only the initial DMS surface binding process that favors silver. The overall energy payoff as the DMS molecules integrate into the surface is even higher than the initial binding advantage for silver as compared to copper, with a 4-12 kJ/mol difference.

This motivation for the formation of silver-containing cluster-like features at the surface would be expected to increase the rate of integration for DMS. and therefore increase the overall rate of the reaction. The average coordination number, or the number of substrate atoms bound to the DMS in the models of **1**, **2**, and **3** models were 2.14, 2.22, and 2.23 respectively, showing that the increased silver content can increase the rate of the reaction during the initial stages. The relationship between the binding energy and the coordination number is summarized below, in Figure 3.7. As the coordination number increases, the binding energy does as well. The large deviation observed in the five-coordinate case is due to the small number of such cases (0.13%).

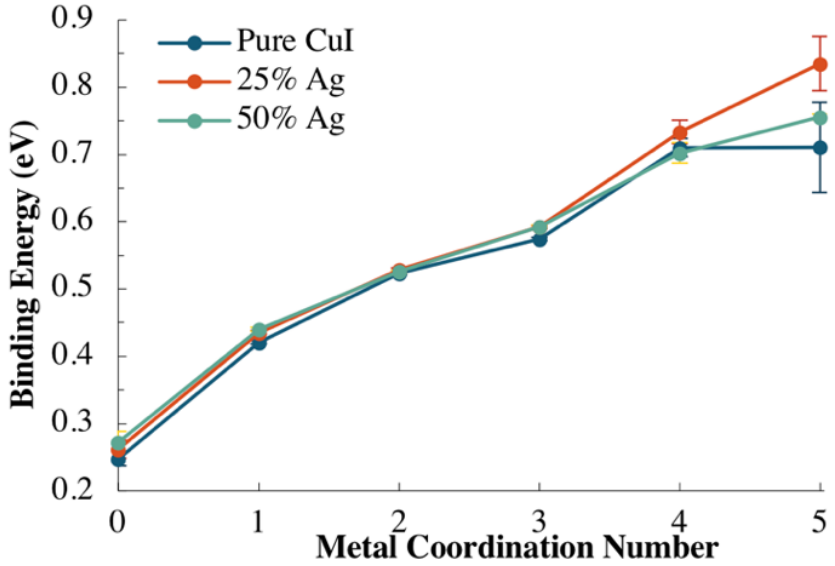

Figure 3.7: DMS binding energy vs. metal coordination number for CuI and CuI/AgI substrates.

Molecular dynamics were also used to simulate the potential reversibility of the reaction. This was done by modeling the interaction of DMS with a 111 surface block of CuI for 5 ns. At approximately room temperature (25 °C) only 5% of the DMS molecules evaporated off of the surface. This number increased to 81% at 120 °C. This observation supports the claim that the DMS-adsorbed samples are fairly stable under air and require additional application of heat or vacuum to fully remove the DMS from the surface. A visual representation of the model of the

surface is shown below in Figure 3.8. A DMS molecule is shown integrating into the surface of the material in the red circle. This is indicative of an intermediate forming on route to the final emissive product.

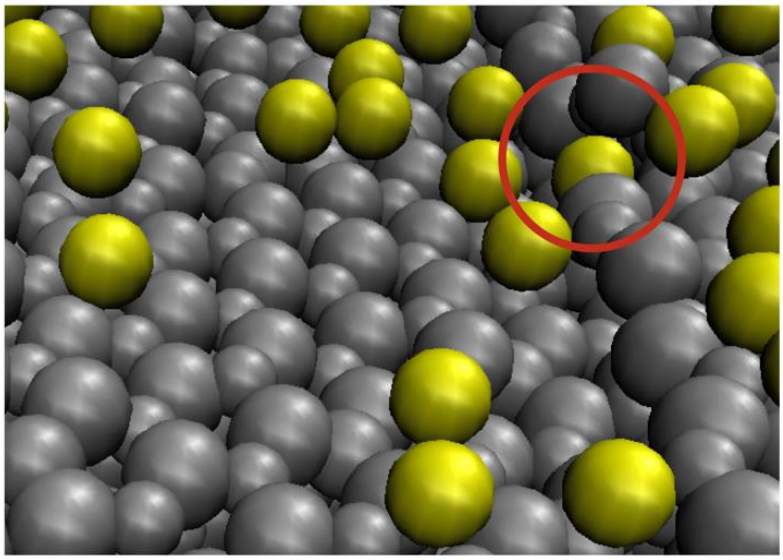

Figure 3.8: Molecular dynamics simulation of DMS on a 111 CuI surface. Methyl groups are omitted and the DMS sulfur atoms are shown as yellow spheres. The substrate atoms are shown as silver spheres. The DMS molecule circled in red is undergoing an embedding process and displacing the substrate atoms in the process. (made with VMD.[32])

The rate of the forward reaction is important, but the stability of the final product is also relevant in this experiment. The timeframe associated with the entire forward reaction sequence is on the order of seconds or a few minutes. In contrast, the reverse reaction takes place over the course of hours, illustrated by an experiment in which a sample of $(CuI)_4(DMS)_3$ was allowed to lose DMS sitting on a bench top in open air (see Figure 3.9). Based on experimental evidence, we can thus assume that the third step in the sequence shown below is non-reversible on the reaction timescale (i.e., $k_3 >> k_{-3}$).

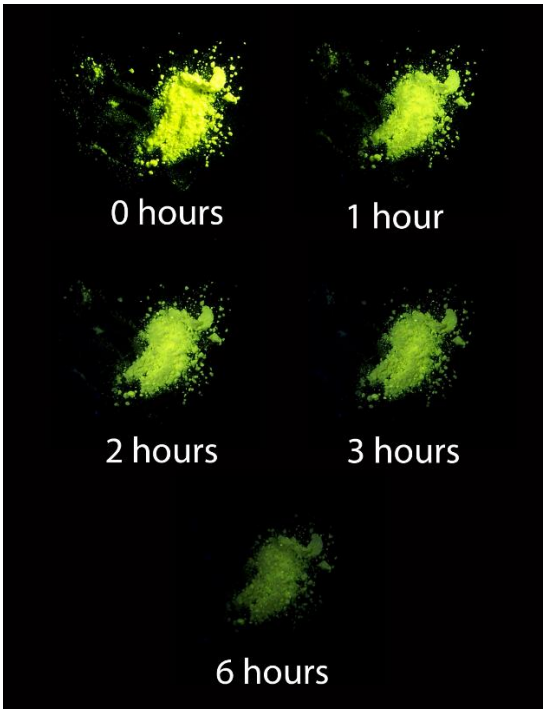

Figure 3.9: Sample **1′** was exposed to open air over time. Images were taken under 365 nm irradiation.

Therefore, with spectroscopic results and molecular dynamics simulation results in hand, an experimental kinetic study of DMS/CuI was undertaken. The kinetics of the system were approached mathematically to provide additional insight to the mechanism of action. Normally, the analysis of the kinetics of a multi-step reaction would be very mathematically complex, but steps were taken in the experimental design to simplify the kinetic analysis. The predicted mechanism is a three-step process as follows:

Step 1: Adsorption of DMS onto the surface of the substrate

Step 2: Embedding/incorporation of DMS into the substrate surface

Step 3: Rearrangement of the substrate into the emissive complex

Or, mathematically,

(1) $$A + B \underset{k_{-1}}{\overset{k_1}{\rightleftarrows}} [A \cdots B]$$

(2) $$[A \cdots B] \underset{k_{-2}}{\overset{k_2}{\rightleftarrows}} [I]$$

(3) $$I \xrightarrow{k_3} P$$

Critically, flooding conditions were used in our experimental setup. This has the effect of dramatically influencing Step 1 via Le Châtelier's principle to shift the equilibrium sharply toward products. Under these conditions, we can assume that the first step, the association of DMS to the surface, happens instantaneously. In this way the formally three-step reaction can be simplified into a two-step reaction. Now the question becomes whether it is Step 2 or Step 3 that is the rate-determining step. Furthermore, the second step is based on the concentration of DMS at the surface, which is being held at an elevated and relatively constant level by the flooding conditions. For this reason, the second step can be assumed to be non-reversible ($k_2 >> k_{-2}$). The value of these reasonable assumptions is they allow a formally very complicated kinetic analysis to be simplified to a series of non-reversible first order reactions. The mathematical analysis required for this is much less intensive, and accuracy is not meaningfully sacrificed. The simplified equation is shown here:

4) $$[A \cdots B] \xrightarrow{k_2} I \xrightarrow{k_3} P$$

The equation:

5) $$[P]_t = [A + B]_0 \left\{1 - \frac{1}{k_3 - k_2}\left\{k_2 e^{(-k_2 t)} - k_1 e^{(-k_3 t)}\right\}\right\}$$

models the appearance of the emissive species [P] and has been solved elsewhere.[33] It is important to note that solution of this equation can give two k values of indeterminate identity. In other words, one solution indicates a quick-forming, weakly emissive intermediate or a slow-forming, strongly emissive intermediate. Given that the mechanism of emission for the

$(CuI)_4(DMS)_3$ is related to the Cu···Cu distance, it is not possible for the strongly emissive intermediate to be forming in the earliest stages of the reaction. Thus, the second step is presumably fast, and the final step (Step 3) is rate-determining.

The experimental setup to measure reaction kinetics was designed to measure the appearance of emission at the 550 nm point as a metric for the reaction rate of the complex, as described in the experimental section. The increase in emission was measured until the surface became saturated and no further change in emission was observed. The results of this experiment are shown below in Figure 3.10.

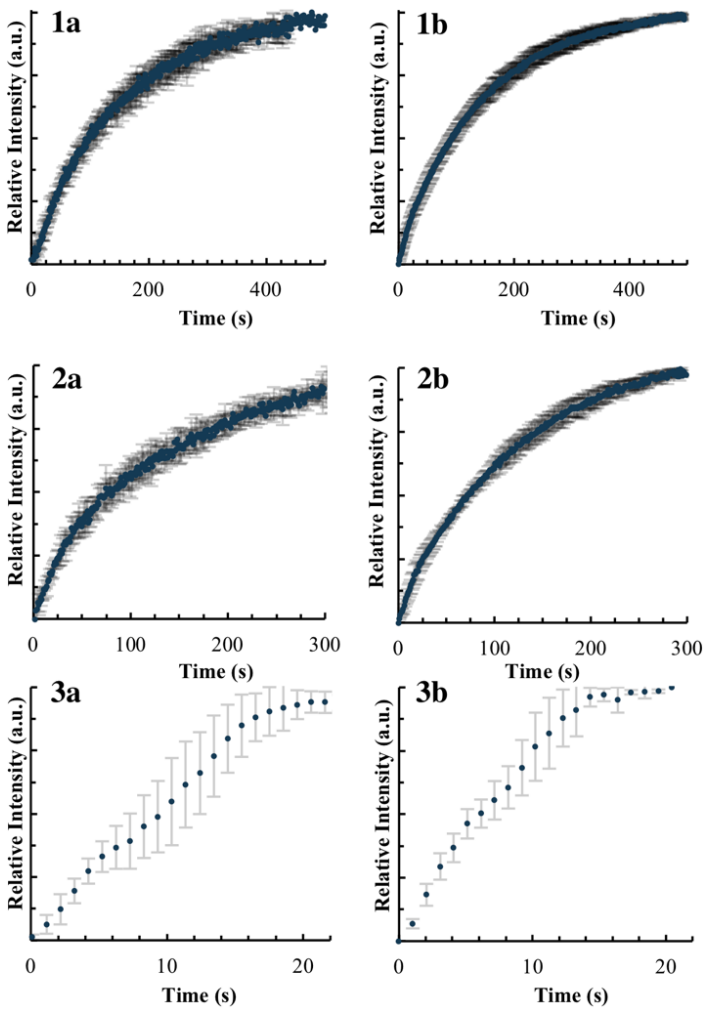

Figure 3.10: Kinetic results for the reaction of DMS with **1**, **2**, and **3** measured at varying DMS flow rates: 43.3 μmol hr^{-1} for the (a) trials and 86.7 μmol hr^{-1} for the (b) trials. The error bars indicate one standard deviation and the graphs are averaged from three trials.

The results from the kinetic experiments show that the rate of reaction increases with increasing silver content, manifesting a particularly significant increase in rate for the 50% silver sample (**3**). Given the shared identity of the final emissive complex, the presence of silver must be accelerating the rate-determining step. The rearrangement rate of the initial DMS-substrate adduct to form the $(CuI)_4(DMS)_3$ is improved for the silver-containing substrates. Despite this kinetic enhancement however, increased Ag-loading lessens the overall degree of reaction. A summary of the kinetics experimental data can be found below in Table 3.1. The summary

supports the previous claims that the rate-determining step is the rearrangement (Step 3) and that increasing heterometallic character increases the rate of that step.

Table 3.1: Summary of kinetics results for **1-3** upon exposure to DMS vapor. Results shown for DMS flow rates of 43.3 μmol hr^{-1} and 86.7 μmol hr^{-1}.

Substrate	Flow Rate	Half-life	k_2	k_3
1	43.3 μmol hr^{-1}	97.7 s	$>10^2$	7.32×10^{-3}
	86.7 μmol hr^{-1}	96.4 s	$>10^2$	7.38×10^{-3}
2	43.3 μmol hr^{-1}	74.2 s	$>10^2$	8.88×10^{-3}
	86.7 μmol hr^{-1}	72.4 s	$>10^2$	8.89×10^{-3}
3	43.3 μmol hr^{-1}	9.85 s	$>10^2$	8.09×10^{-2}
	86.7 μmol hr^{-1}	6.14 s	$>10^2$	8.19×10^{-2}

The foregoing work offers a detailed mechanistic analysis of the process of vapochromism in copper-based materials. This analysis has shown that the rate-determining step of the reaction is the rearrangement that must occur to transition from the tightly packed γ-CuI to the structure of the emissive product. Incorporation of silver into the substrate did not alter the zinc blende structure of the material. Further, both kinetic and molecular dynamics calculations support the benefits of having heterometallic character to improve the rate of the reaction. The agreement here lends validity to the proposed mechanism of (1) adsorption, (2) integration, and (3) rearrangement. Incorporating heterogeneous metals can increase the binding affinity of the incoming nucleophile and as a result increase the reaction rate. This work

should prove valuable for those attempting to increase the speed and effectiveness of vapochromic materials, and particularly those working with d^{10} metals. The further insight provided by this work makes it possible to approach optimization of these materials with the mechanism of action in mind and an initial improvement with the heterometallic results.

4) Investigation into Exchange Compounds:

The work on CuAgI heterometallic materials as chemical sensors in the previous chapter resulted in several important findings. Although the work clearly showed the functionality of CuI as a chemical sensor, the rate of the reaction leaves something to be desired. With reaction times in the many seconds or minutes range, the practicality of the potential sensor is called into question. With regard to this issue, one of the most important findings of the previous chapter concerned the rate-determining step of the reaction. The preceding mechanistic study revealed that the lengthiest time component involved the rearrangement of the dense zinc blende CuI to produce the emissive cluster. Specifically, CuI "chunks" must be broken off of the main mass in order to react to the incoming nucleophile and form the tetramer product. This being the rate-determining step (RDS), it is the obvious target for optimization and research aimed at improving the performance of of the detector material. A clear option for improvement would be to tune the material so as to increase the rate of reaction at the RDS. Therefore, we opted to pursue a variation of CuI(L) that would more easily undergo reaction with nucleophiles to produce the emissive tetramer product. An detector material that consists of a "pre-formed" cubane tetramer (or other Cu_xI_x cluster) would solve in advance the issue of reconstructing the dense CuI network. In essence the reaction would be reduced to that of a simple ligand exchange. Such reactions are known for CuI and would hopefully provide an associated increase in reaction rate with nucleophiles[34]. A diagram outlining the intended process is shown below in Scheme 4.1.

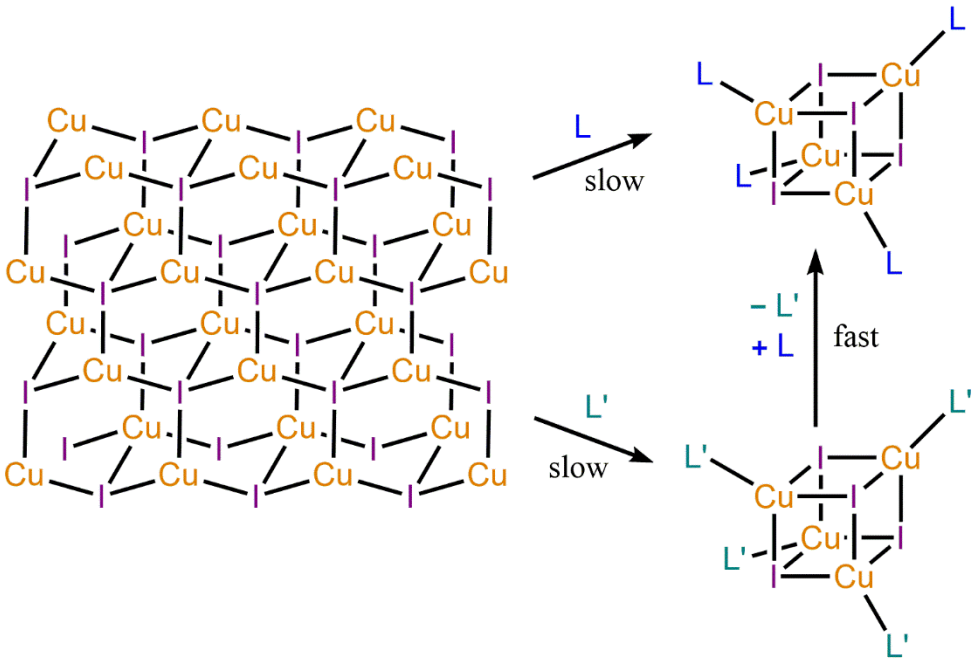

Scheme 4.1: The conversion of zinc blende CuI to product.

The key to enacting the process shown in Scheme 4.1 is the identification of a suitable exchange ligand, L′. There are several features that are desirable in a good L′ ligand. The ligand should bind strongly enough that it can form a stable complex with CuI, but be sufficiently weakly binding that it can be easily displaced by an incoming nucleophile. A reasonable starting point for a ligand is the well-documented copper(I)-binding ligand pyridine.[27] This ligand can be customized with one or more electron-withdrawing groups (EWG) in order to lower its binding strength. Secondly, the ligand of choice should be as non-volatile as possible. This characteristic would allow the ligand to remain present for the regeneration of the material by removal of the volatile incoming nucleophile. Finally, the CuI(L′) complex should be weakly emissive or ideally non-emissive. Limited emission from the unreacted detector material would optimize its limit of detection by removing potential spectral interference from unreacted starting material.

With all this in mind, we set out to study the copper(I) iodide coordination of a series of pyridine ligands substituted with EWGs. The list of ligands tested is as follows: 2-cyanopyridine (2-PyCN), 3-cyanopyridine (3-PyCN), 4-cyanopyridine (4-PyCN) and 3-nitropyridine (3-$PyNO_2$).

The substituents chosen (CN, NO_2) were intended to draw electron density from the aromatic ring and so by induction and resonance deactivate the nitrogen in the ring. Prior to our work, two complexes utilizing the above ligands were known: $(CuI)_2(3\text{-}PyCN)_4$ and $(CuI)_4(4\text{-}PyCN)_5$.[35] The former is a rhomboid dimer and the latter is a chain of tetrameric units that are bridged at the 4 position CN group (see below). In addition to replicating these known compounds, in the course of the following work we discovered six other novel complexes. The crystal structures of the known complexes were redetermined alongside three new CuI complexes of 2-PyCN, one new CuI complex of 3-PyCN, and two new isomeric $CuI(3\text{-}PyNO_2)$ structures.

We set out to synthesize CuI complexes of 2-PyCN, 3-PyCN, 4-PyCN and $3\text{-}PyNO_2$. There are well documented methods for the synthesis of CuI(X-Py) compounds in the literature including concentrated aqueous KI solution[35], in acetonitrile[36], with CuI in organic suspension[37], and via ligand exchange reactions in organic solvent. To most thoroughly explore the full range of potential products, all of the above were tested with the exception of ligand exchange. Given our intention of making a complex that is readily subject to ligand exchange with loss of the EWG-Py ligand, it seemed quite unlikely that ligand exchange would be a favorable route for synthesis of such complexes.

The previously unexplored 2-PyCN system proved to be surprisingly complicated. An early experiment where a solution of CuI and 2-PyCN in acetonitrile (MeCN) was allowed to slowly evaporate produced three different crystal structures in three different CuI-to-ligand ratios. The complexes were distinguished by emission under black light and visual appearance/habit of the crystals. The resulting structures were solved as $(CuI)_2(2\text{-}PyCN)_4$ (**1**), CuI(2-PyCN) (**2**), and $(CuI)_3(2\text{-}PyCN)$ (**3**). The first compound to crystallize at the early stages of the evaporation experiment was compound **1**. The bulk of material produced as the experiment subsequently continued was a mixture of **2** and **3**, with **3** seeming to form in greater amount. When allowed to proceed to dryness, a mottled solid appearing to be a mixture of **3** and CuI was produced. Given the results of the evaporation study, it is not surprising that isolating each of these compounds in

pure form proved difficult. Initial tests using concentrated aqueous KI solutions gave products that proved to be inevitably contaminated with leftover KI. Crystallization attempts of CuI/2-PyCN solutions from MeCN tended to strongly favor compound **3**, and even more so in low temperature crystallizations. Quite surprisingly, **3** was favored even in conditions wherein ligand was used in excess. As a result, **3** was readily produced in pure form from an optimized MeCN crystallization method. During synthesis, a trace amount of an unidentified black product was observed when ligand was added to a solution of CuI. This unknown product was always carefully filtered out before crystallization.

The apparent thermodynamic stability of **3** made synthesis of pure **1** and **2** very challenging. Given the propensity of **3** to form out of MeCN solutions, a neat synthesis in 2-PyCN was pursued. The low melting point of 2-PyCN made it possible to carry out this synthesis at mild temperatures (30 °C). The resulting product was analyzed and identified as pure **1**. Compound **2** has not been synthesized in pure form yet. The tendency for **3** to form and leave behind a solution that is rich in ligand was a major obstacle to making this compound. Attempted comproportionation reactions in both the suspension and solid state produced exclusively mixtures of the three products. Even though **2** was not isolated in pure bulk form, its crystal structure was solved from crystals isolated as part of the evaporation experiment described above.

Two unique products were formed from the reaction of CuI with 3-PyCN. Both products were synthesized in MeCN by controlling the CuI-to-ligand ratio. The previously reported (CuI)(3-PyCN) (**5**) was synthesized using a 1:1 CuI to 3-PyCN ratio and the novel dimer $CuI_2(3\text{-PyCN})_4$ (**4**) was synthesized at a 1:2 CuI to 3-PyCN ratio. Reacting CuI with 4-PyCN produced only one compound, the known $(CuI)_4(4\text{-PyCN})_5$(**6**).[38] The interesting stoichiometry here stems from the hybrid role of the ligand in both terminal and bridging capacities. This compound could be made from either the concentrated aqueous KI method or from MeCN.

Synthesis using 3-$PyNO_2$ and CuI produced two unique compounds with the same stoichiometry (1:1). When a MeCN solution of CuI and 3-$PyNO_2$ at a 1:1 ratio was slowly cooled, an orange product that would be solved as a cubane tetramer $(CuI)_4(3\text{-}PyNO_2)_4$ (**7**) was produced. Higher reactant concentration at reflux temperature in MeCN produced a red stair step polymer $(CuI)(3\text{-}PyNO_2)$ (**8**) upon rapid cooling. Although **7** could be reliably synthesized in pure form, the synthesis method for **8** could also produce amounts of **7.** Simply recrystallizing **8** from MeCN could resolve this problem. Recrystallization was particularly effective if a seed crystal of **8** was used to encourage that product to form. Although diethyl ether was used often in the PyCN syntheses to precipitate or wash products, addition of diethyl ether to solutions of CuI and 3-$PyNO_2$ precipitated only CuI. It is likely that the weak coordinating strength of this ligand combined with its solubility in ether were to blame for this behavior.

Thermogravimetric analysis (TGA) was used to further analyze the products of the above syntheses. Compounds **1**, **3**-**8** displayed clean loss of ligand at temperatures below 200 °C, leaving CuI. A sample trace is shown below, in Figure 4.1.

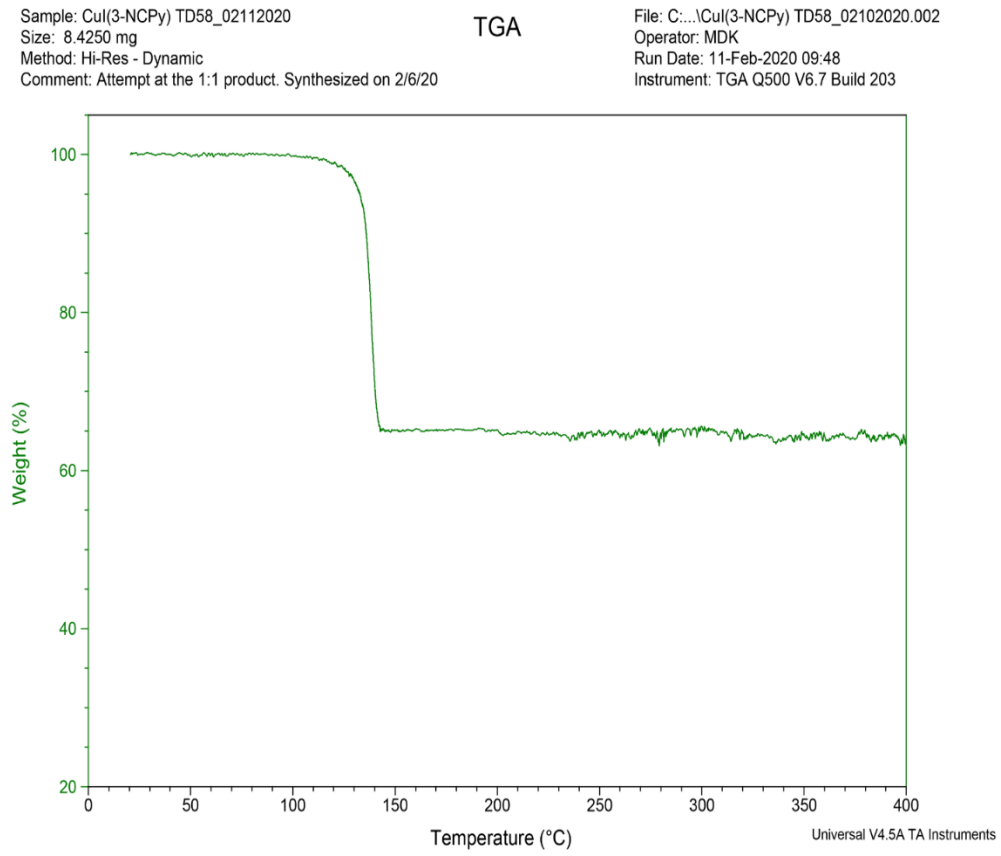

Figure 4.1: TGA analysis of **5**.

Complexes **1** and **4** each evidence an additional plateau during their decomposition, as shown in Figure 4.1 above. The trace for **1** is shown below in Figure 4.2.

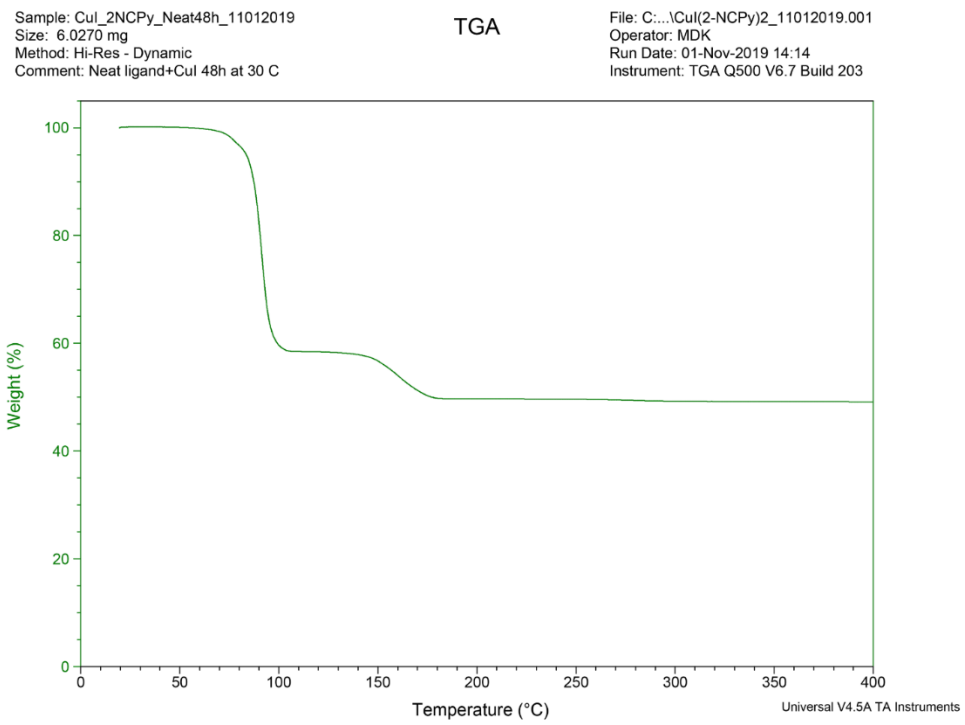

Figure 4.2: TGA trace of **1**

Mass loss calculations indicate that the plateau observed above corresponds to a conversion from **1** to **3**. The three-step reaction, then, would be:

$$(CuI)_2(PyCN)_4 \rightarrow 2\ CuI(PyCN) + 2\ PyCN \quad (1)$$

$$3\ CuI(PyCN) \rightarrow (CuI)_3(PyCN) + 2\ PyCN \quad (2)$$

$$(CuI)_3(PyCN) \rightarrow 3\ CuI + PyCN \quad (3)$$

So **1** decomposes to **3** via a combination of reactions (1) and (2) and then follows the general trend going straight to CuI via reaction (3). It is interesting to note that no corresponding plateau was observed for **2** in this study. That supports the synthetic findings that **2** has limited stability. The other ligand-rich compound, **4**, also showed a small plateau corresponding in mass percent to the 1:1 product, **5**, i.e. the analog of reaction (1). Each of the other tested compounds decomposed directly to CuI.

Given the end goal of identifying a potential exchange compound, the luminescence behavior of the CuI-PyCN and CuI-3-$PyNO_2$ compounds was of great interest. Ideally, the ligand

exchange would manifest a significant and easily observable difference in emission. The solid state emission of the various compounds produced herein was tested under UV irradiation at ambient temperature. Shown below in Figure 4.3 are photographs of each of the isolated compounds **1**, **3**-**8** under visible light and under 365 nm irradiation. All but one of the isolated PyCN compounds were fairly emissive, with a couple being very strongly emissive. Notably compound **2**, which was not isolated in bulk, appeared quite dim under 365 nm irradiation. Of additional note are the 3-$PyNO_2$ compounds, which showed no visible emission under 365 nm irradiation. This makes them prime candidates for ligand exchange.

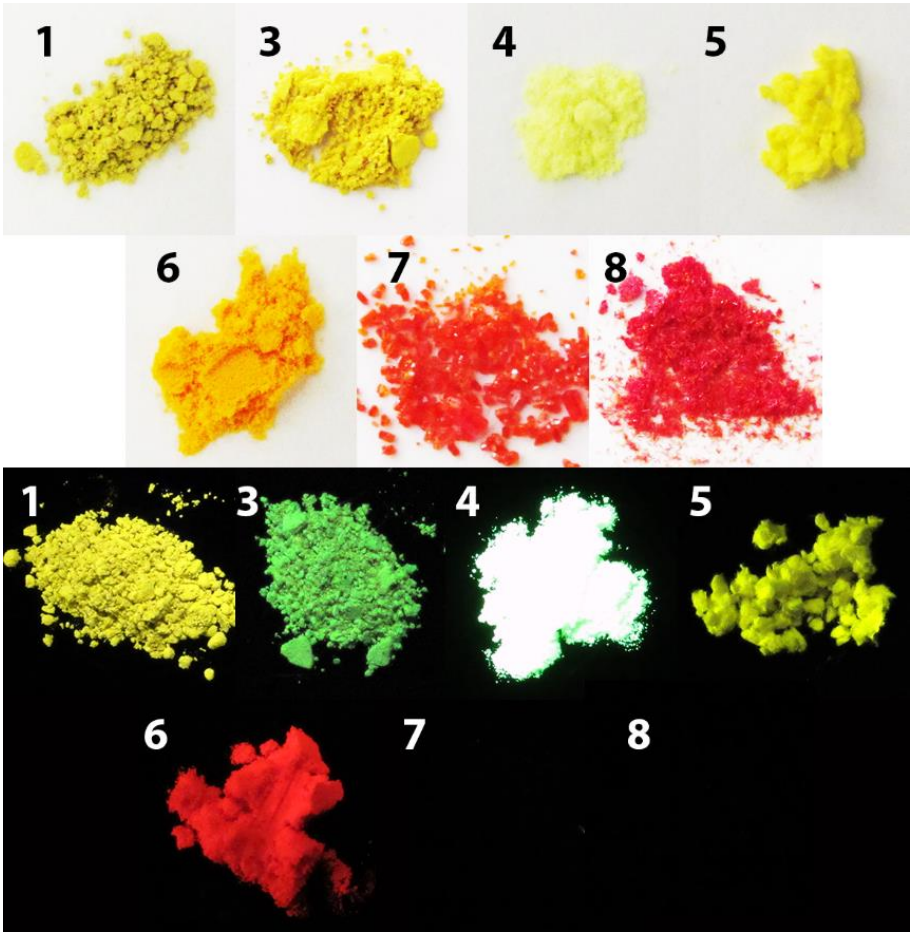

Figure 4.3: Photos of isolated compounds, top: visible light, bottom: 365 nm irradiation.

Room temperature luminescence spectra were collected for the isolated compounds (**1, 3-6**) that showed observable emission. Compounds **7** and **8** were also tested, but showed no emission above the baseline as room temperature. The emission spectra corresponded to visual observations, with the maxima occurring between 500-600 nm evidenced as broad peaks. The spectra are shown below in Figure 4.4.

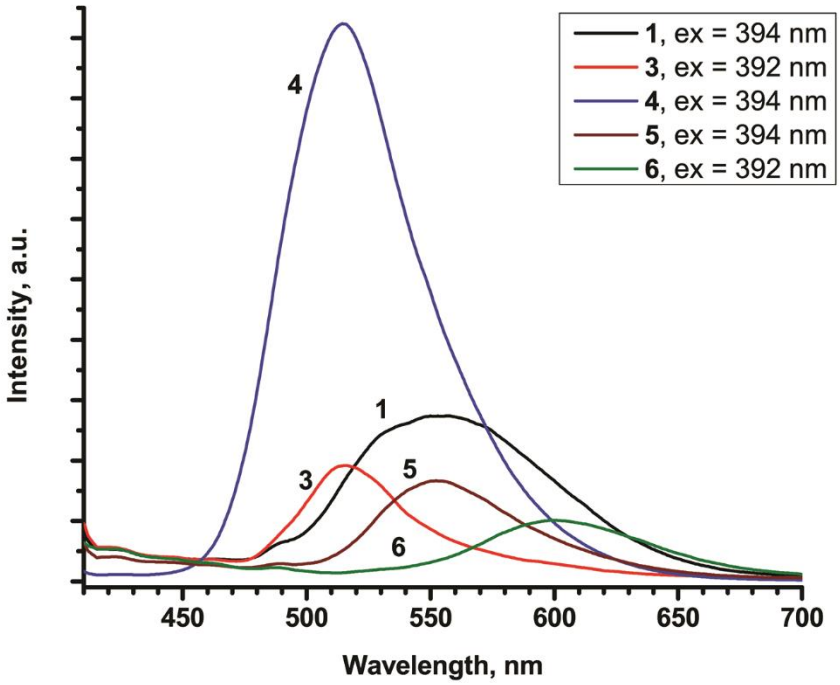

Figure 4.4: Emission spectra of **1**, **3-6** at **1** (λ_{ex} = 394 nm, λ_{em} = 555 nm), **3** (λ_{ex} = 392 nm, λ_{em} = 516 nm), **4** (λ_{ex} = 394 nm, λ_{em} = 514 nm, detector set at lower voltage to prevent saturation), **5** (λ_{ex} = 394 nm, λ_{em} = 552 nm), and **6** (λ_{ex} = 392 nm, λ_{em} = 601 nm).

The emission intensity of **4** was found to be substantially above that of the other tested samples. The large emission bands in CuI complexes bound to aromatic ligands have been historically attributed to either mixed halide/metal-to-ligand charge transfer (XMLCT) or cluster-centered charge transfer transitions[31]. Furthermore, the excitation spectra show great similarity between the compounds with each consisting of a broad, weak band in the 390-395 nm range. This behavior agrees with previously reported compounds of this type. The strong similarity suggests that the photophysical behavior is the same for each compound, and is most likely a XMLCT

process. The strength of cyano as an electron-withdrawing group lowers the energy of the acceptor π* orbital of the pyridine through both induction and resonance and therefore lowers the corresponding XMLCT. This same logic can be applied to the nitropyridine, and yet no emission is observed. It is likely the emission would appear in a similar spectral region, but a quenching mechanism of some kind is preventing radiative recombination.

Crystal structures were solved for all the reported complexes, and the structure types are illustrated below in Scheme 4.2. Crystal solution data are provided in Table 4.1, and selected bond lengths and angles are available in Table 4.2. Powder X-ray diffraction (PXRD) data were also collected for each isolate compound. These traces matched well with the PXRD data that were calculated from the single crystal structures. Generally, the complexes determined are structurally familiar for CuX-L family, but with two of the structures being unique. The complexes range in stoichiometry from ligand-rich in **1** and **4**, and **6** to even in **2**, **5, 7**, and **8** to a highly unusual ligand-poor complex **3**. Both **3** and **6** (although **6** has been reported previously) are structurally unique in the literature. The nature of the nitrogen in the cyano group makes this ligand potentially bidentate, which behavior is noted in two cases.

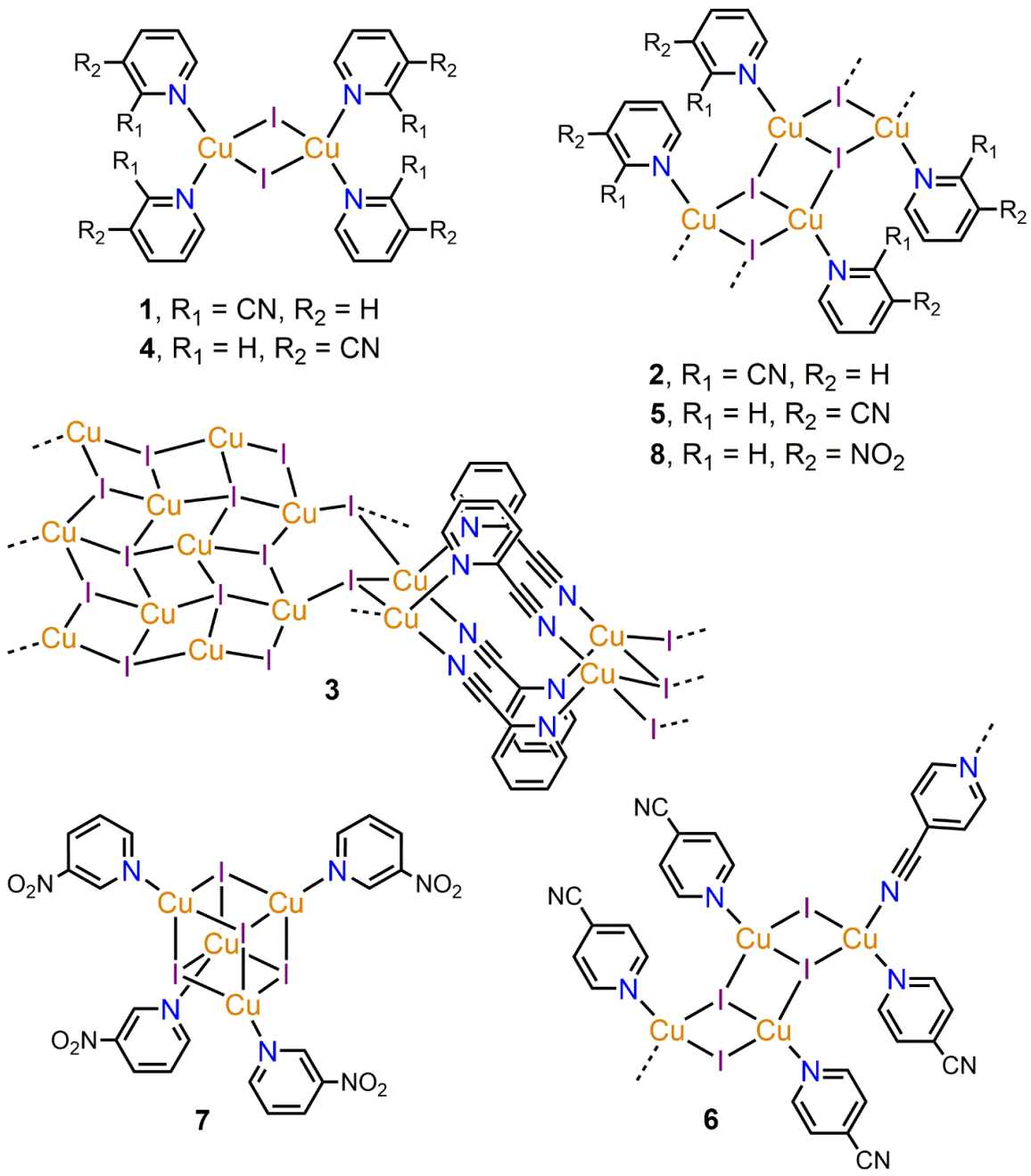

Scheme 4.2: Structures of reported complexes within

Commencing our structural discussions with the ligand-rich 1:2 CuI:PyCN complexes, both $(CuI)_2(2\text{-PyCN})_4$ (**1**) and $(CuI)_2(3\text{-PyCN})_4$ (**4**) are molecular rhombic dimers built around a central Cu_2I_2 rhomboid dimer unit (Figure 4.5). Compound **1** crystallized as yellow plates that solved in non-centrosymmetric orthorhombic space group *Pnn2* at room temperature, while

undergoing a reversible phase change to monoclinic below about 250 K. Compound **4**, which represents a 100 K redetermination of a known structure[36] crystallized as yellow plates and solved in the centrosymmetric triclinic space group *P*−1. Both compounds **1**, which is centered on a C2 axis, and **4**, which lies on an inversion center, are half crystallographically independent. Pyridine-coordinated CuI dimers such as **1** and **4** are well established[36]. In many cases, including **1** and **4**, the two 4-coordinate copper centers are separated by less than the 2.85 Å Cu···Cu van der Waals radius sum. Nevertheless, compound **1** stands out for a very large N−Cu−N angle of 122.86(17)°. This large value apparently results from the steric interaction between the cyano groups on adjacent 2-PyCN ligands, and have been noted with other 2-substituted pyridine or pyrazine ligands.[39] Most other $(CuI)_2(RPy)_4$ complexes show nearly tetrahedral N−Cu−N angles comparable to that of **4**, 108.06(6)°. Compound **1** appears to be the only $(CuI)_2(RPy)_4$ species that shows *both* a large N−Cu−N angle and a short Cu···Cu distance. Finally, it should be noted **1** shows a very low crystal density (the lowest in this study, 1.904 g cm^{-3}), again presumably due to expansion of the structure as a result of sterically induced twisting.

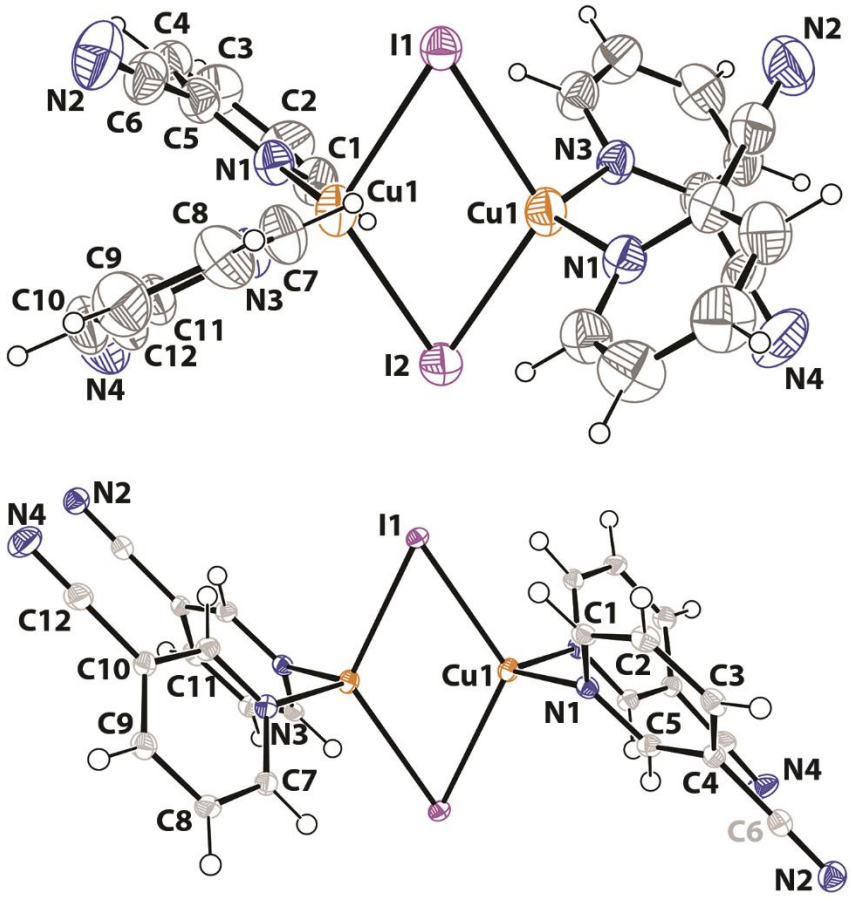

Figure 4.5. Thermal ellipsoid drawings of **1** (30% ellipsoids, top) and **4** (50% ellipsoids, bottom).

The remaining ligand-rich complex reported here is a 100 K redetermination of $(CuI)_4(4\text{-}PyCN)_5$ (**6**)[39], see Figure 4.6. The compound crystallized in the centrosymmetric monoclinic space group $P2_1/c$, proving to be half independent about an inversion center. The Cu_4I_4 core may be regarded either as a trio of edge-sharing Cu_2I_2 rhombs, a truncated CuI stair step, or an open cubane cluster. The interplanar angle between an outer rhomb and the central rhomb is 60.5°. There are close Cu···Cu interactions across the outer rhomb (Cu1···Cu2 = 2.6837(14) Å) and across the central rhomb (Cu2···Cu2 = 2.784(2) Å), both of which are within the van der Waals radius sum. The ligands decorate and bridge the Cu_4I_4 cores in unique fashion. While a monodentate 4-PyCN is coordinated to both independent Cu atoms, an additional bidentate bridging 4-PyCN connects a pair of Cu1 atoms on adjacent clusters, producing a 1-D polymer.

This bidentate ligand bonds through both the Py and CN nitrogen atoms. Such bridging behavior is well recognized for this ligand.[40] The bridging 4-PyCN ligand in **6** is symmetrically disordered insofar as the single Cu1 is coordinated to one Py N associated with its terminal 4-PyCN ligand and one Py/CN N atom associated with the bridging 4-PyCN ligand . The terminal 4-PyCN rings along a chain are aligned and π-stacked (C1···centroid and C4···centroid distances = 3.615 Å, 3.741 Å). The pyridine rings of the two independent terminal ligands are nearly coplanar (1.6° interplanar angle) and both are at nearly 90° angles to the bridging ligand ring. The chains pack together running parallel to one another and to the *c*-axis. Adjacent chains alternate with respect to the positions of the clusters and bridges along the chain. The sterically demanding cluster region of one chain is aligned with the flat bridging ligand of the next chain. The cluster arrangement $Cu_4I_4L_6$ is unusual. A single known complex that forms this unit without the influence of chelating ligands is $(CuI)_4(2\text{-MePy})_6$.[41]

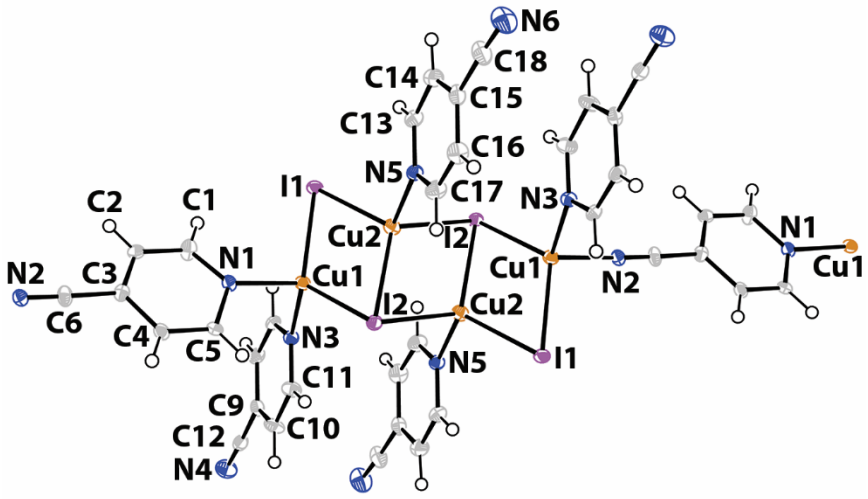

Figure 4.6. Thermal ellipsoid (50%) drawing of **6**. Disorder in bridging 4-PyCN ligand omitted.

The 1:1 compounds produced fell into either of two common CuI-L categories: (CuI)(2-PyCN) (**2**), (CuI)(3-PyCN) (**5**), and $(CuI)(3\text{-PyNO}_2)$ (**8**) were infinite ladders, and $(CuI)_4(3\text{-PyNO}_2)_4$ (**7**) was a cubane tetramer. The structures are shown in Figure 4.7. Ladder complexes **2** and **5** (both yellow needles) each crystallized in triclinic space group *P*−1, but were not isomorphic. Nevertheless, along with complex **8**, which crystallized in the monoclinic space group $P2_1/c$, they

were isostructural. The red blades of **8** showed two-position disorder for the NO_2 group (54:46 ratio). In **2**, **5**, and **8** Cu_2I_2 rhombs share edges to create zigzag stair step arrangements, which are decorated at each Cu center with a single pyridine ligand. As is the case with all rhomb-based structures reported herein, all Cu atoms are 4-coordinate, and the Cu−I−Cu angles within the rhombs are highly acute (*ca.* 61−67°) while those without are obtuse (*ca.* 98−110°). In contrast the I−Cu−I angles within the rhombs and those without are similar to one another, being relatively close to the tetrahedral value (*ca.* 98−119°). Cuprophilic Cu···Cu distances of <3.0 Å are present in all three cases. The structure of orange block crystal **7**, which crystallizes in the non-centrosymmetric tetragonal group $P-42_1/c$, was that of a $(CuI)_4(3\text{-}PyNO_2)_4$ cubane. Such structures are well-established[42] and are isomeric to the ladder forms described above. However, rather than consisting of an infinite polymer, the ladder closes upon itself to form a cyclic tetramer. Due to the geometrical constraints cubanes show only internal rhomb Cu−I−Cu and I−Cu−I angles. As is typically the case for this structural type, the distorted cube geometry forces greater distortion in the structural parameters: Cu−I−Cu angles within the rhombs for **7** are 57.702(16)−59.346(15)°, and the Cu···Cu distances are 2.5891(9) and 2.6518(7) Å. The crystal structure **7** is isomorphic with the piperidine analog $(CuI)_4(piperidine)_4$.[43]

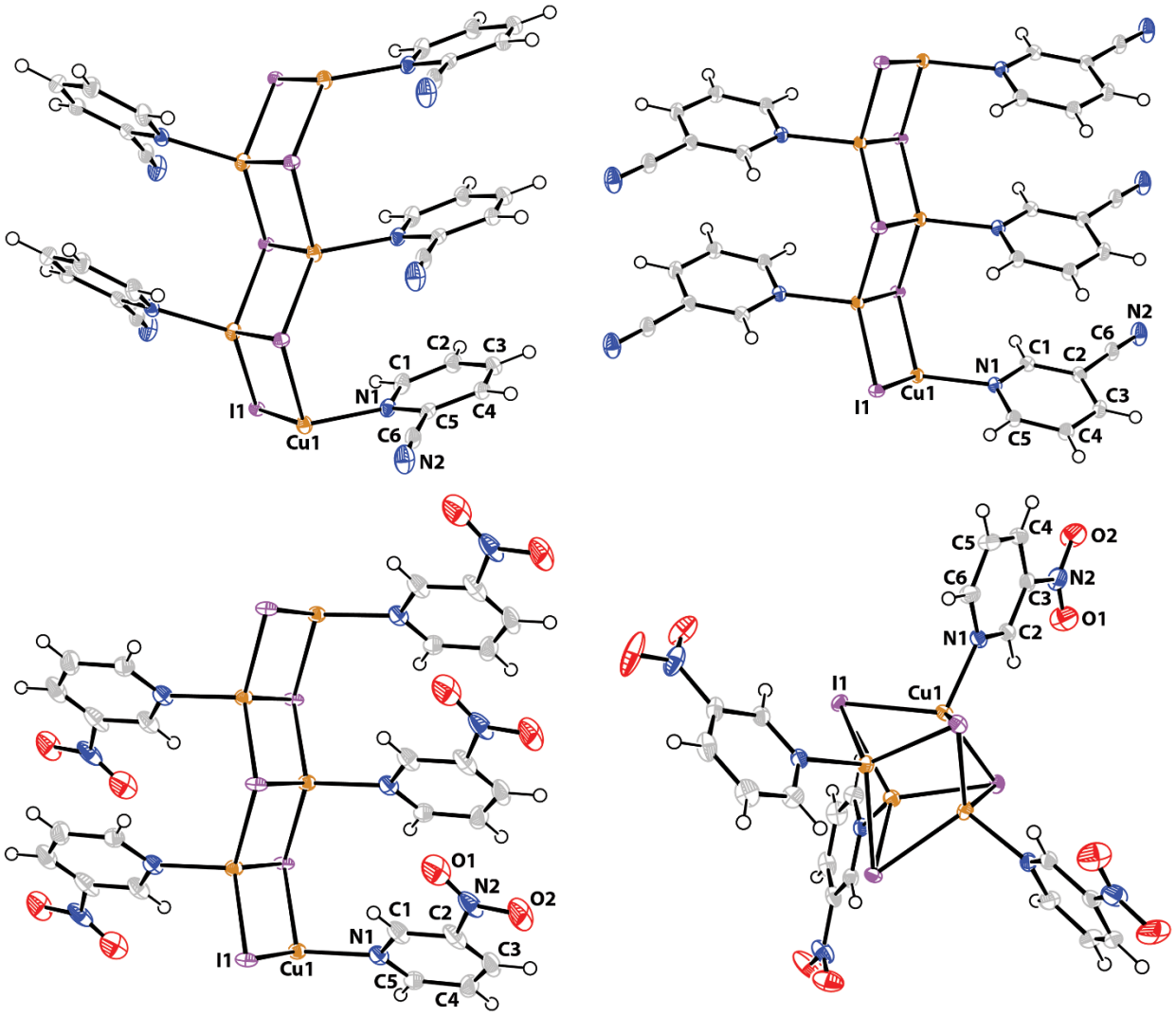

Figure 4.7. Thermal ellipsoid (50%) drawings of (clockwise) **2**, **5**, **7**, and **8**. Disorder in 3-$PyNO_2$ in **8** is omitted.

The only copper-rich compound identified in the current study was the 3:1 CuI:2-PyCN species **3**. This unique compound crystallized as brightly emissive yellow needles, solving in the triclinic space group *P*−1. Crystals of **3** invariably showed two-component twinning based on 180° rotation about the (100) normal. Standard twinning solution and refinement methods were employed successfully to produce a good quality, ordered structure, which is depicted in Figure 4.8. The unprecedented 2-D structure is constructed from two connected motifs. The first of these

consists of a series of cyclic dimers in which pairs of 2-PyCN ligands bridge pairs of Cu atoms that are part of a $Cu_\infty I_\infty$ zigzag chain. The bridging 2-PyCN ligands are oriented with respect to one another in a C2 rotation fashion, and while oriented in parallel fashion, are too far apart to be considered π-stacked (centroid···centroid >4 Å). Stacks of these $Cu_2I_2(2\text{-PyCN})_2$ units run parallel to the crystallographic *a*-axis. The second motif in the structure is an infinite triple stair step structure $(Cu_4I_4)_\infty$ consisting of a repeat unit of three edge-sharing rhombs that share edges with the next trio, and so on. While the inner Cu atom in the resulting zigzag sheet (Cu3) is 3-coordinate, the outer Cu2 is 4-coordinate since it also bonds to the iodide (I1) associated with the dimers, i.e. motif 1. The ribbons associated with motifs 1 and 2 both propagate parallel to the crystallographic *a*-axis and have similar widths parallel to the *b*-axis: 10.72 Å (C2···C2 in motif 1) and 9.62 Å (I1···I3 in motif 2). Thus, the zigzag ribbon that runs parallel the c-axis is roughly 10−11 Å in thickness. Alternatively, the sequences $(\ldots Cu1{-}I1\ldots)_\infty$, $(\ldots Cu2{-}I3\ldots)_\infty$, $(\ldots Cu3{-}I2\ldots)_\infty$, $(\ldots Cu3{-}I2\ldots)_\infty$, $(\ldots Cu2{-}I3\ldots)_\infty$, and $(\ldots Cu1{-}I1\ldots)_\infty$ can viewed as six parallel zigzag CuI chains. As part of the junction between motifs 1 and 2, cyclohexane-like rings are formed from (−Cu1−I1−Cu2−I3−Cu2−I1−).

Bridging behavior has been herein demonstrated in two CuI-PyCN phases: **3** and **6**. Both of these complexes show a good degree of chemical stability. In the case of 4-PyCN, **6** is the only phase that has been observed and, while multiple phases are noted with 2-PyCN, **3** forms most readily. It seems likely that the evolution of these phases is aided by the formation of soluble clusters. In the case of **6**, it is readily conceivable that tetramer $Cu_4I_4(4\text{-PyCN})_4$ forms in solution and is then knit into an insoluble polymer by an additional ligand. For **3**, ready formation of soluble $Cu_2I_2(2\text{-PyCN})_2$ ring units could drive product formation, offering a robust template about which the truncated CuI network can form. In this light it is interesting that no bridging behavior has been found for 3-PyCN. We have previously demonstrated bridging behavior for all three isomers of PyCN and dicyanobenzene with $Cu(BF_4)$.[41] While the *ortho*-bridging ligands form dimer units reminiscent of that in **3**, and the *para*-bridging ligands form linear polymers in related fashion to

6, the *meta*-bridging behavior differs for 3-PyCN (trimer) and *m*-dicyanobenzene (polymer). The lack of a clear networking preference for the *meta*-bridge might militate against stable bridging behavior in the CuI-3-PyCN system.

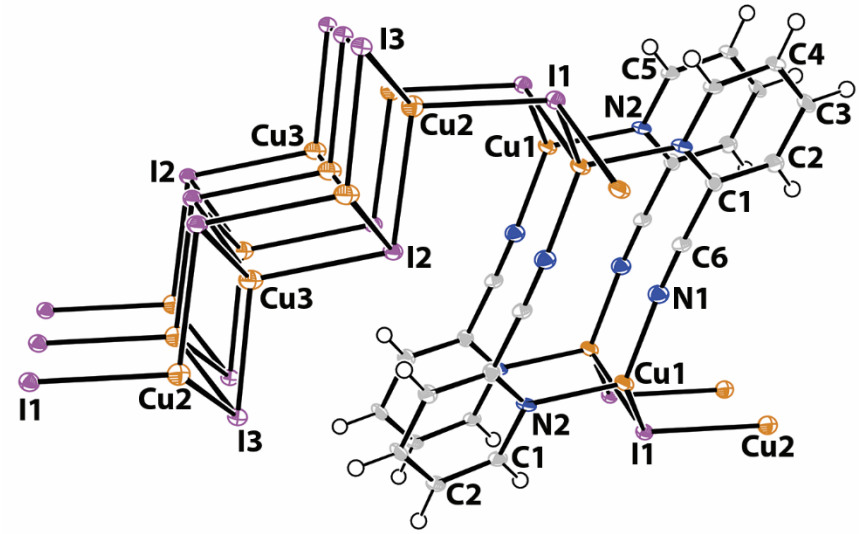

Figure 4.8. Thermal ellipsoid (50%) drawing of **3**.

In summary, reported herein are the syntheses and structural analyses of CuI complexed with cyanopyridine (X-PyCN) and 3-nitropyridine (3-$PyNO_2$). In total 6 new structures were determined and two previously reported structures were retdetermined. Structures of 2-PyNC included a dimer $(CuI)_2(2\text{-PyCN})_4$, the stair step (CuI)(PyCN) that could be isolated in bulk, and the unprecedented $(CuI)_3(2\text{-PyCN})$ in which $(Cu_4I_4)_\infty$ ribbons were linked together by $(Cu_2I_2)(2\text{-PyCN})_2$ dimers. The complexes of 3-PyCN are the dimer $(CuI)_2(3\text{-PyCN})_4$ and the stair step (CuI)(3-PyCN). A single complex is found from 4-PyCN in polymeric form $(CuI)_4(4\text{-PyCN})_5$. Two compounds of identical stoichiometry are found from the reaction of 3-$PyNO_2$, the cubane $(CuI)_4(3\text{-PyNO}_2)$ and the stair step $(CuI)(3\text{-PyNO}_2)$. Each of the isolated X-PyCN complexes were quite strongly emissive from a mixed halide/metal to ligand charge transfer. Curiously, the 3-$PyNO_2$ complexes show no observable emission at room temperature, making them the strongest

candidates for a sensing material that operates using an exchange mechanism with pyridine and other soft nucleophiles. Exploration of the applicability for this material in an aqueous environment as a sensor for pyridine is ongoing.

Table 4.1. Crystal and Structure Refinement Data.

complex	**1**	**2**	**3**	**4**
CCDC deposit no.	1990786	1990787	1990788	1990789
color and habit	yellow block	yellow needle	yellow needle	yellow plate
size, mm	0.14 × 0.14 × 0.08	0.52 × 0.06 × 0.04	0.42 × 0.04 × 0.03	0.18 × 0.15 × 0.05
formula	$C_{24}H_{16}Cu_2I_2N_8$	$C_6H_4CuIN_2$	$C_6H_4Cu_3I_3N_2$	$C_{24}H_{16}Cu_2I_2N_8$
formula weight	797.33	294.55	675.43	797.33
space group	*P*nn2 (#34)	$P2_12_12_1$ (#19)	*P*−1 (#2)	*P*−1 (#2)

a, Å	12.0420(3)	4.1422(2)	4.16810(10)	8.0808(4)
b, Å	12.7905(3)	12.9712(7)	11.3567(3)	8.8571(5)
c, Å	9.0291(2)	14.3290(8)	12.7439(4)	9.5425(5)
α, deg	90	90	94.2970(10)	91.6840(10)
β, deg	90	90	95.334(2)	95.7620(10)
γ, deg	90	90	98.867(2)	108.7420(10)
volume, Å^3	1390.69(6)	769.89(7)	591.01(3)	642.12(6)
Z	2	4	2	1
ρ_{calc}, g cm^{-3}	1.904	2.541	3.795	2.062
F_{000}	760	544	600	380
μ(Mo Kα), mm^{-1}	19.543[b]	6.765	67.478[b]	4.090
temperature, K	296(2)	100(2)	100(2)	100(2)
residuals:[a] R; R_w	0.0263; 0.0764	0.0126; 0.0303	0.0272; 0.0602	0.0140; 0.0360
goodness of fit	1.097	1.130	1.074	1.035
Flack	0.023(10)	0.038(13)	−	−

[a]R = $R_1 = \Sigma||F_o| - |F_c||/\Sigma|F_o|$ for observed data only. $R_w = wR_2 = \{\Sigma[w(F_o^2 - F_c^2)^2]/\Sigma[w(F_o^2)^2]\}^{1/2}$ for all data. [b]Cu radiation data.

Table 4.1. Cont'd.

complex	**5**	**6**	**7**	**8**
CCDC deposit no.	1990790	1990791	1990792	1990793
color and habit	yellow needle	yellow needle	orange block	red prism
size, mm	0.67 × 0.08 × 0.06	0.58 × 0.25 × 0.11	0.19 × 0.10 × 0.09	0.53 × 0.12 × 0.03

formula	$C_6H_4CuIN_2$	$C_6H_5Cu_2N_5S_2$	$C_{20}H_{16}Cu_4I_4N_8O_8$	$C_5H_4CuIN_2O_2$
formula weight	294.55	641.16	1258.17	314.54
space group	*P*–1 (#2)	$P2_1/c$ (#13)	$P-42_1c$ (#114)	$P2_1/c$ (#13)
a, Å	4.1179(3)	10.1529(3)	14.6149(6)	4.1494(5)
b, Å	7.5645(5)	12.0739(4)	14.6149(6)	26.144(3)
c, Å	12.4451(7)	15.0326(5)	7.7887(3)	7.5660(9)
α, deg	96.8670(10)	90	90	90
β, deg	95.5150(10)	101.0090(10)	90	100.564(2)
γ, deg	97.6560(10)	90	90	90
volume, $Å^3$	378.97(4)	1808.86(10)	1663.63(15)	806.86(17)
Z	2	4	2	4
ρ_{calc}, g cm^{-3}	2.581	2.354	2.512	2.589
F_{000}	272	1196	1168	584
μ(Mo Kα), mm^{-1}	6.872	5.771	6.287	6.482
temperature, K	100(2)	100(2)	100(2)	100(2)
residuals:[a] R; R_w	0.0135; 0.0344	0.0448; 0.1057	0.0114; 0.0315	0.0234; 0.0451
goodness of fit	1.081	1.553	1.321	1.277
Flack	−	−	0.027(5)	−

[a]$R = R_1 = \Sigma||F_o| - |F_c||/\Sigma|F_o|$ for observed data only. $R_w = wR_2 = \{\Sigma[w(F_o^2 - F_c^2)^2]/\Sigma[w(F_o^2)^2]\}^{1/2}$ for all data.

Table 4.2. Selected bond distances (Å) and angles (deg) for all complexes.

1	**2**	**3**

Cu–I	2.638(4), 2.681(4)	2.5998(5), 2.6311(4), 2.6837(5)	2.5930(9)−2.6913(9)
Cu–N_{Py}	2.070(4), 2.077(4)	2.078(3)	2.070(5)
Cu–N_{cyano}	−	−	1.935(5)
Cu···Cu	2.8117(15)	2.9076(6), 2.9076(6)	2.8075(12), 2.8948(12), 2.9211(17)
Cu–I–Cu	63.24(11),[a] 64.41(12)[a]	67.535(12),[a] 66.324(12),[a] 103.244(14)	62.88(3)[a]−81.83(3),[a] 103.39(3)−109.56(3)
I–Cu–I	116.17(3)	103.245(15), 111.675(17),[a] 114.437(18)[a]	98.17(3)[a]−115.58(3),[a] 99.94(3)−117.53
I–Cu–N	102.9(2), 103.3(3), 105.3(3), 107.0(2)	120.78(9), 107.58(8), 97.61(8)	96.73(13), 107.51(13), 109.97(15), 117.28(14)
N–Cu–N	122.86(17)	−	118.9(2)

[a]Angle within rhomb; other angles are outside rhomb.

Table 4.2. Cont'd.

	4	**5**	**6**
Cu–I	2.6440(3), 2.6480(3)	2.6162(3), 2.6399(3), 2.6600(3)	2.6010(11)−2.6914(12)
Cu–N_{Py}	2.0680(16), 2.0724(16)	2.0648(18)	2.043(7), 2.082(7)

$Cu–N_{cyano}$	−	−	2.069(8)
Cu···Cu	2.6373(5)	2.6865(5), 2.7883(5)	2.6837(14), 2.784(2)
Cu–I–Cu	59.782(9)[a]	61.475(10),[a] 63.484(11),[a] 102.604(11)	61.78(3),[a] 61.08(3),[a] 98.06(4)
I–Cu–I	120.218(9)[a]	102.603(11), 116.517(10),[a] 118.526(10)[a]	103.83(4), 117.30(4),[a] 119.06(4),[a] 117.22(4)[a]
I–Cu–N	105.96(4)−107.79(4)	102.48(5), 105.05(5), 110.60(5)	100.9(2)−113.9(2)
N–Cu–N	108.06(6)	−	99.1(6)

[a]Angle within rhomb; other angles are outside rhomb.

Table 4.2 Cont'd.

	7	**8**
Cu–I	2.6706(5), 2.6860(5), 2.6949(5)	2.6415(6), 2.6257(6), 2.6440(6)
$Cu–N_{Py}$	2.031(3)	2.059(3)
$Cu–N_{cyano}$	−	−
Cu···Cu	2.5891(9), 2.6518(7)	2.6968(10), 2.8420(10)
Cu–I–Cu	57.702(16),[a] 59.051(15),[a] 59.346(15)[a]	61.357(18),[a] 65.272(18),[a] 103.957(19)
I–Cu–I	111.837(16),[a] 112.609(16),[a] 116.124(17)[a]	103.959(19), 114.729(18),[a] 118.643(18)[a]

I–Cu–N	103.13(8), 105.22(8), 106.70(9)	102.54(9), 107.12(9), 109.51(10)
N–Cu–N	−	−

[a]Angle within rhomb; other angles are outside rhomb.

5) **Exchange Compound Testing**

The results of the preceding study highlighted $(CuI)_4(3\text{-}PyNO_2)_4$ (**7**) as a promising exchange material for use as a chemical sensor. For the next step, a two pronged approach mirroring the previously described CuAgI nanoparticles was developed. The two avenues of exploration would be computational analysis and experimental work to investigate the sensing capacity of the material. The computational study would attempt to uncover the thermodynamic and kinetic aspects of the substitution reaction, while looking further into the unusual non-emissive behavior of the complex. To fully realize this approach both DFT and molecular mechanics methods will be explored. The experimental approach will focus primarily on the effectiveness of this material in aqueous environments as a suspension. The vapochromic behavior of copper(I) complexes is well-documented, but performance in water less well known. The behavior of the exchange complex can be directly compared to that of pure CuI to determine whether there is a noticeable difference between the two in terms of reaction rate and limit of detection.

Pyridine (Py) was chosen as the nucleophile for initial testing. There are several advantages for pyridine in this capacity. It is very similar in structure to our bound ligand but is a binds more strongly due to the absence of the electron-withdrawing nitro substituent. Pyridine is also readily available and is water miscible, making it a natural fit for aqueous testing. The cubane complex formed with CuI, Py $(CuI)_4(Py)_4$, is brightly yellow emissive, which makes detection of the forming product possible not only by instrumental means but also by simple visual inspection. Ensuring that both the exchangeable compound, $(CuI)_4(3\text{-}PyNO_2)_4$, and the exchanged product, $(CuI)_4(Py)_4$, are cubane structures can simplify computations, since assuming that the cluster structure is unaffected by the reaction it can further ease computational demands by necessitating only minor structural changes to the computational model.

In our computational investigation we set out to answer two broad questions. 1) What is the mechanism of the exchange? and 2) What is causing the absence of emission? In theory, the exchange of ligand can follow one of two paths: A mechanism reminiscent of an S_N1 would involve

initial loss of the exchangeable ligand, followed by filling of the vacancy by the incoming ligand. An S_N2 type reaction would first have the incoming ligand bind and the exchangeable ligand depart thereafter. S_N1 and S_N2 mechanisms for the first reaction step in the exchange sequence of **7** with pyridine is shown in Scheme 5.1.

Scheme 5.1: The proposed reactions of **7** with Py.

S_N1: $[(CuI)_4(3\text{-}PyNO_2)_4] \rightarrow [(CuI)_4(3\text{-}PyNO_2)_3] + 3\text{-}PyNO_2$

$[(CuI)_4(3\text{-}PyNO_2)_3] + Py \rightarrow [(CuI)_4(3\text{-}PyNO_2)_3(Py)]$

S_N2: $[(CuI)_4(3\text{-}PyNO_2)_4] + Py \rightarrow [(CuI)_4(3\text{-}PyNO_2)_4(Py)]$

$[(CuI)_4(3\text{-}PyNO_2)_4(Py)] \rightarrow [(CuI)_4(3\text{-}PyNO_2)_3(Py)] + 3\text{-}PyNO_2$

The intermediate species proposed in either case, $[(CuI)_4(3\text{-}PyNO_2)_3]$ for S_N1 and $[(CuI)_4(3\text{-}PyNO_2)_4(Py)]$ for S_N2 might be either a true intermediate with a finite lifetime, or a transition state. The first exchange step only is shown in Scheme 4.1. The reaction would presumably proceed in like fashion following this first step until all of the $3\text{-}PyNO_2$ ligands were replaced by the much more strongly binding Py ligand. A DFT study was conducted by our collaborator Dr. Aaron Nicholas at George Washington University. To test the preference for a S_N1 reaction versus a S_N2 reaction two systems from the reaction progress were evaluated. DFT works best when dealing with thermodynamics and energy. DFT is not as well suited to kinetics and the mechanics of a chemical reaction. This caveat is why the analysis by DFT can seem convoluted or over complicated.

In the modelling of the S_N1 reaction system, the relative stabilities of the various partially Py-substituted intermediate structures were assessed. As one might expect, the simulations show that $3\text{-}PyNO_2$ ligand dissociation produces an increase in complex energy, and subsequent

coordination of the incoming Py yields a lower energy complex. The reaction coordinate for the complete four-step process is shown, in Figure 5.1.

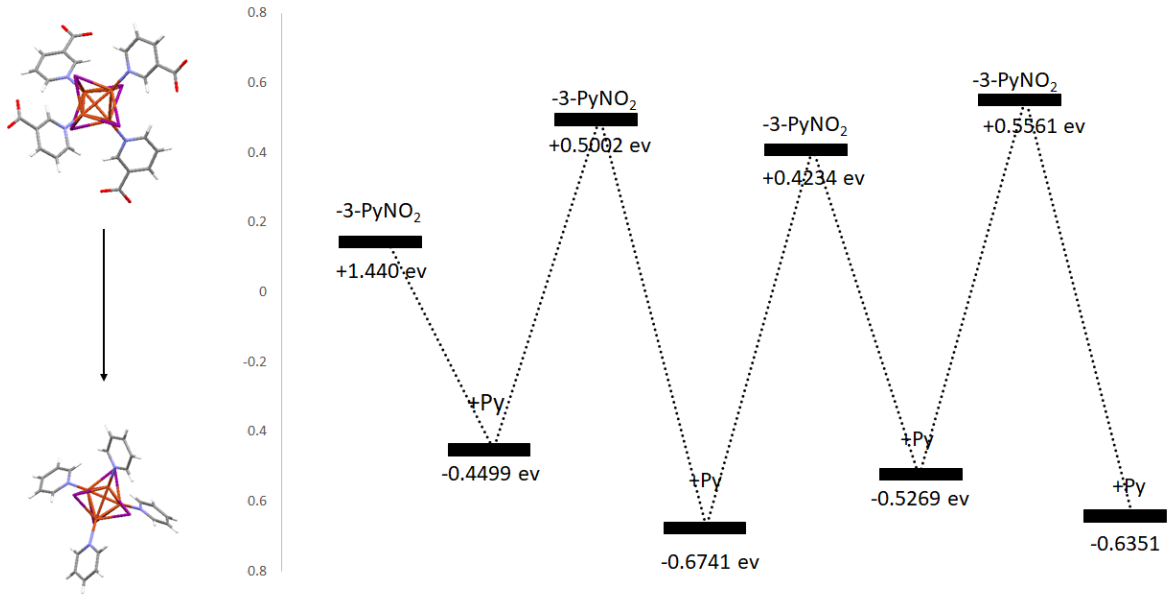

Figure 5.1: DFT predicted energies for each reaction step in the conversion of $(CuI)_4(3\text{-}PyNO_2)_4$ to $(CuI)_4(Py)_4$.

This finding has several important implications. First, it supports the preliminary experimental and theoretical work suggesting that Py is a stronger ligand for the CuI system than the $3\text{-}PyNO_2$ ligand. The more insightful finding is that further substitution appears to occur with a smooth energy transition to the final product. This allows for some model simplification in the proposed mechanism for an S_N1 type reaction. Another very important piece of information is that the $3\text{-}PyNO_2$ ligand is soluble in water. This would theoretically improve the favorability of the S_N1 type reaction by providing a stabilizing influence to a departing ligand. While this computational study does not affirm that the reaction is S_N1 like, it suggests that such a reaction mechanism is certainly possible.

Computational modelling of the S_N2 system also involved the modelling of a sequence of intermediate structures. Initially, a structure of **7** with a Py molecule in close proximity to the cluster was optimized. This process led to a structure with the Py ligand becoming bound and the 3-$PyNO_2$ ligand being ejected from the cluster. In an attempt to find the probable transition state that should exist in an S_N2 mechanism, Dr. Nicholas locked the bond distances to force the cluster to attain a five coordinate system. When the optimization was attempted the cluster began to disassemble with the five-coordinate copper center releasing one of its iodide bonds, thus returning it to the favored four-coordination.

These simulations, again, yield some interesting points. As before, these results support the idea that pyridine is strong enough as a ligand to displace the 3-$PyNO_2$. While the simulation seems to support that this can occur in a relatively synchronous process, the transition state itself is less clear. There are a few reasons for why this is inconclusive. Optimizing a structure that is very high in energy can lead to unrealistic behavior, such as the iodide release observed here. With that in mind, five-coordinate Cu(I) complexes are extremely rare. These factors combined are much more supportive of a dissociative mechanism than one initiated by nucleophilic attack.

The second question to be addressed concerns the surprising lack of emission by **7**. This is a puzzling occurrence since related Cu(I) cubanes are typically quite emissive. The simple $(CuI)_4Py_4$ cubane is very brightly emissive. Moreover, as noted in Chapter 2 even with a different strong electron-withdrawing group on Py (e.g. PyCN) the resulting cubane can still be strongly emissive. Furthermore, the bright orange color of **7** under visible light seems to suggest photophysical activity. As previously mentioned, $(CuI)_4L_4$ cubanes typically have a high energy (HE) and low energy (LE) emission band.[45] One possibility for the lack of emission is that the room temperature HE band is perhaps pushed out into the near IR by the lowering of the ligand HOMO due to the electron-withdrawal of the nitro group. One would certainly expect that the presence of the nitro group would significantly lower the ligand orbital energies. A second possibility is that the nitro group specifically is a major source of vibrations, which could allow the

non-radiative (thermal) relaxation of the excited state. To help probe this uncertainty, an optimization of the excited state structure was carried out. Such an excited state simulation is extremely resource intensive and it not yet complete, but so far the results indicate noticeable extension in the bond lengths of the nitro group in the excited state. The extension of these bonds indicate vibrational activity would be suggestive of a vibrational relaxation mechanism from the excited state back to the ground state without photon emission. This finding would be in keeping with literature on the topic, wherein nitro groups have been noted to quench emission[46] in organic polymers and metal organic frameworks.

Experimental excitation/emission scans extending into the IR were carried out to test the possibility that the emission bands(s) of **7** were simply red-shifted. Although not strong, the emission patterns observed match the standard cubane system with a high energy band dominating at low temperature and a lower energy band at higher temperature. This experiment effectively rules out the possibility of shifted emission into the IR and further supports the idea that the absence of observable emission stems from the vibrational relaxation capabilities of the ligand nitro group.

While computational studies can offer insight, having an experimental basis is very helpful for contextualizing the theoretical mechanistic results. With this in mind, experimental studies were undertaken to study the rate of reaction and the limit of detection for aqueous Py using CuI and **7** as sensing materials. To enhance the potential applications of the proposed sensing materials, aqueous testing environments were employed. The goal was to evaluate the Py reaction rates for pure CuI vs the exchange compound **7**. In theory the exchange compound should react more rapidly by the process proposed above where preforming the structure of the exchange will increase the rate of reaction.

The reaction conditions for the experiments required using a suspension of the water insoluble solid sensing materials. In order to minimize variation in the properties of the solid, the samples were well ground before use and massed to ensure comparable reaction capacity.

Pyridine is miscible in water and so solutions of Py in a variety of concentration were prepared. The aqueous Py solutions were added to the solid sensing material with stirring for preliminary testing of the reaction progress. The yellow-green fluorescence of the $(CuI)_4(Py)_4$ cubane at 545 nm was monitored to assess the reaction progress.

Initial experiments involving CuI were done with visual observation under black light (365 nm) to determine if the reaction would even take place in water. At high concentrations of pyridine (100 mM) the reaction resulted visible emission of the suspended solid within one minute of addition. This solution was quite concentrated for sensor work, and so an effort was made to find a preliminary limit of detection (LOD) for CuI as a proof of concept for moving forward with more detailed aqueous testing. The results of an order of magnitude dilution series is shown below, in Figure 5.2.

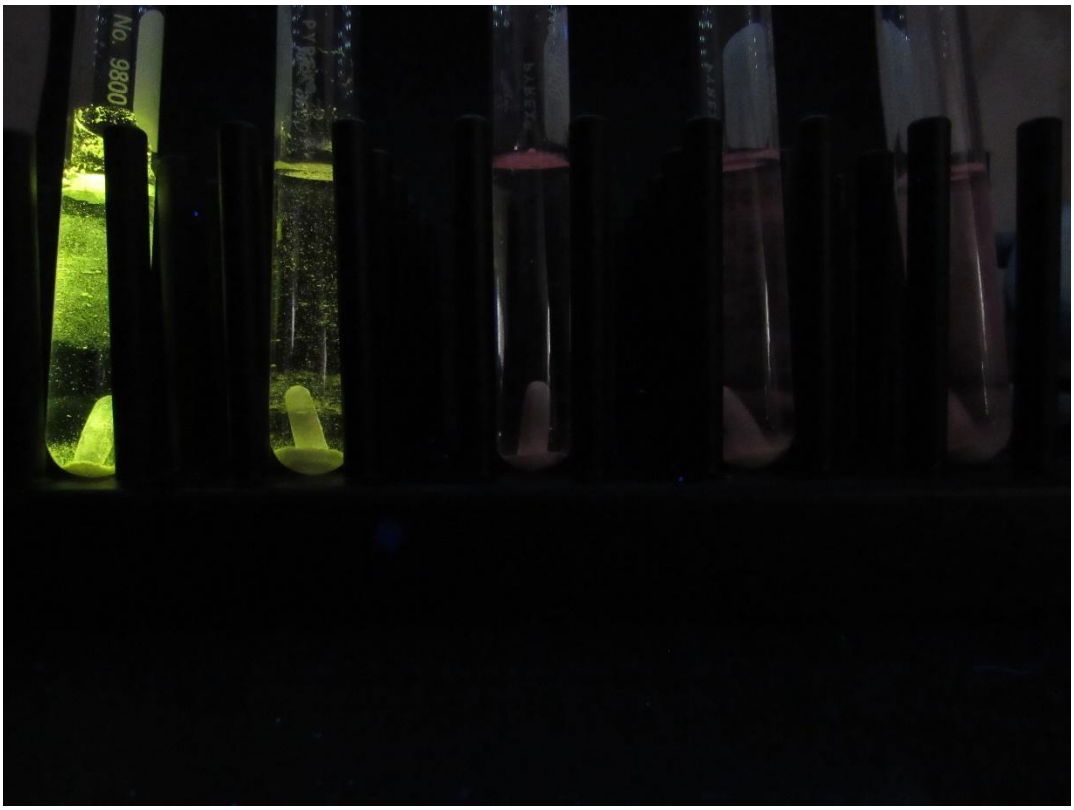

Figure 5.2: Suspensions of CuI in aqueous pyridine photographed under 365 nm irradiation after 24 h stirring time. From left: [Py] = 100 mM, 10 mM, 1 mM, 0.1 mM, 0.01 mM.

The visual study offers several important preliminary results. There is a clearly visible difference between the samples that have undergone a reaction (100, 10 mM) that show bright yellow green emission and the ones that still show the dim pink-purple emission of CuI itself. Thus, there is clear potential for these materials as visual Py concentration detectors in aqueous media. Furthermore, the study indicates that the LOD for CuI lies somewhere between 1-10 mM.

To better study the reaction taking place, a commercial fluorimeter was used to measure the emission of the sample. To establish baseline results, a series of blanks were collected on the instrument to contextualize the results. Chosen as blank materials were pure water, an aqueous suspension of 100 mm alumina (to test light scattering from an unreactive solid), an aqueous suspension of CuI, and an aqueous suspension of exchange compound **7**. The results of these blank trials are shown in Figure 5.3.

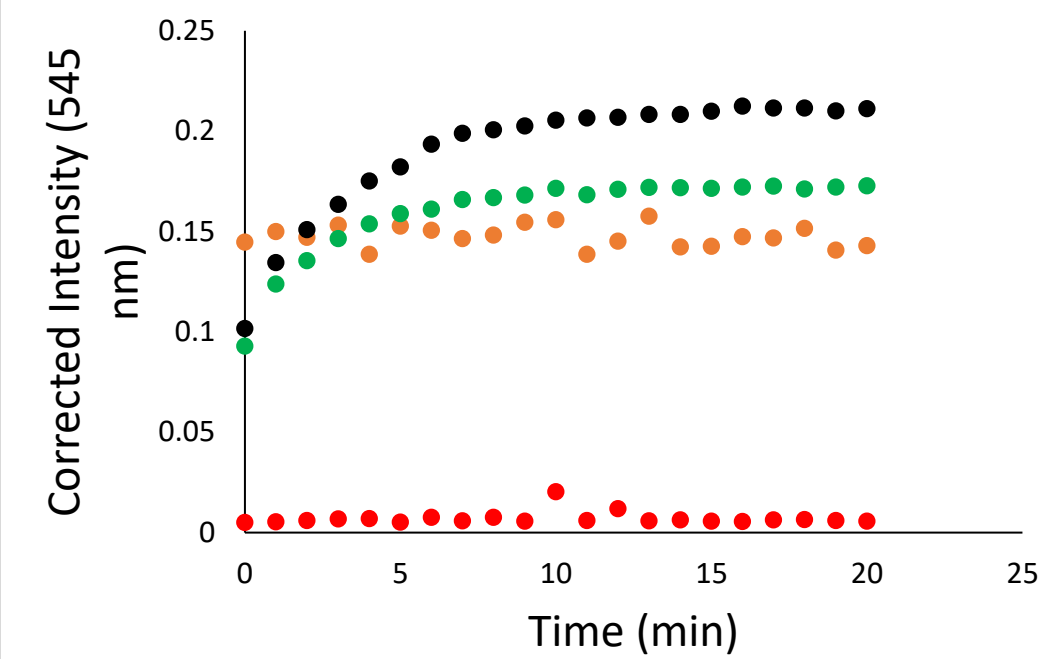

Figure 5.3: Fluorescence response of blanks (excitation = 365 nm, emission = 545 nm): DI water (red), alumina in water (orange), **7** in water (green) and CuI in water (black).

The blank scans were corrected using quinine as an internal standard in solution. The results for the alumina, which is non-emissive, show an elevated baseline. This is likely due to the light scattering of fluorimetry using a suspension. Also of note is the behavior of both CuI and **7** in water which displayed similar increasing emission signal that flattened out between 5-10 minutes after addition of the solid to water.

The two samples were then compared to one another by doing multiple trials at 10 mM Py. The results of that study are shown below, in Figure 5.4.

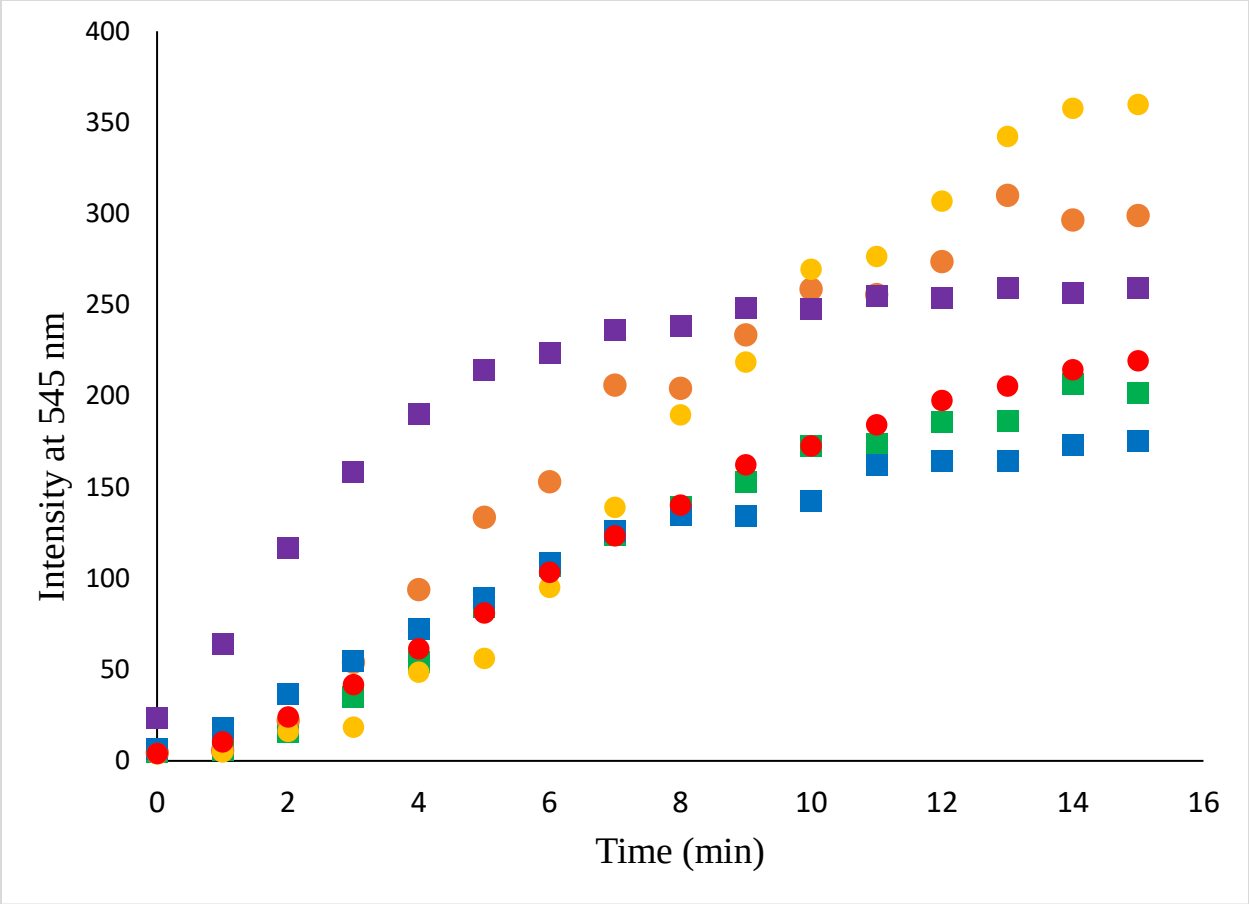

Figure 5.4: Fluorescence emission response (excitation = 365 nm, emission = 545 nm) for CuI (squares) and **7** (circles) in 10 mM Py (aq).

To further investigate the properties of the exchange compound in water, a sample of **7** was placed in a test tube and allowed to sit undisturbed at room temperature for 24 h. The resulting TGA is given below in Figure 5.5.

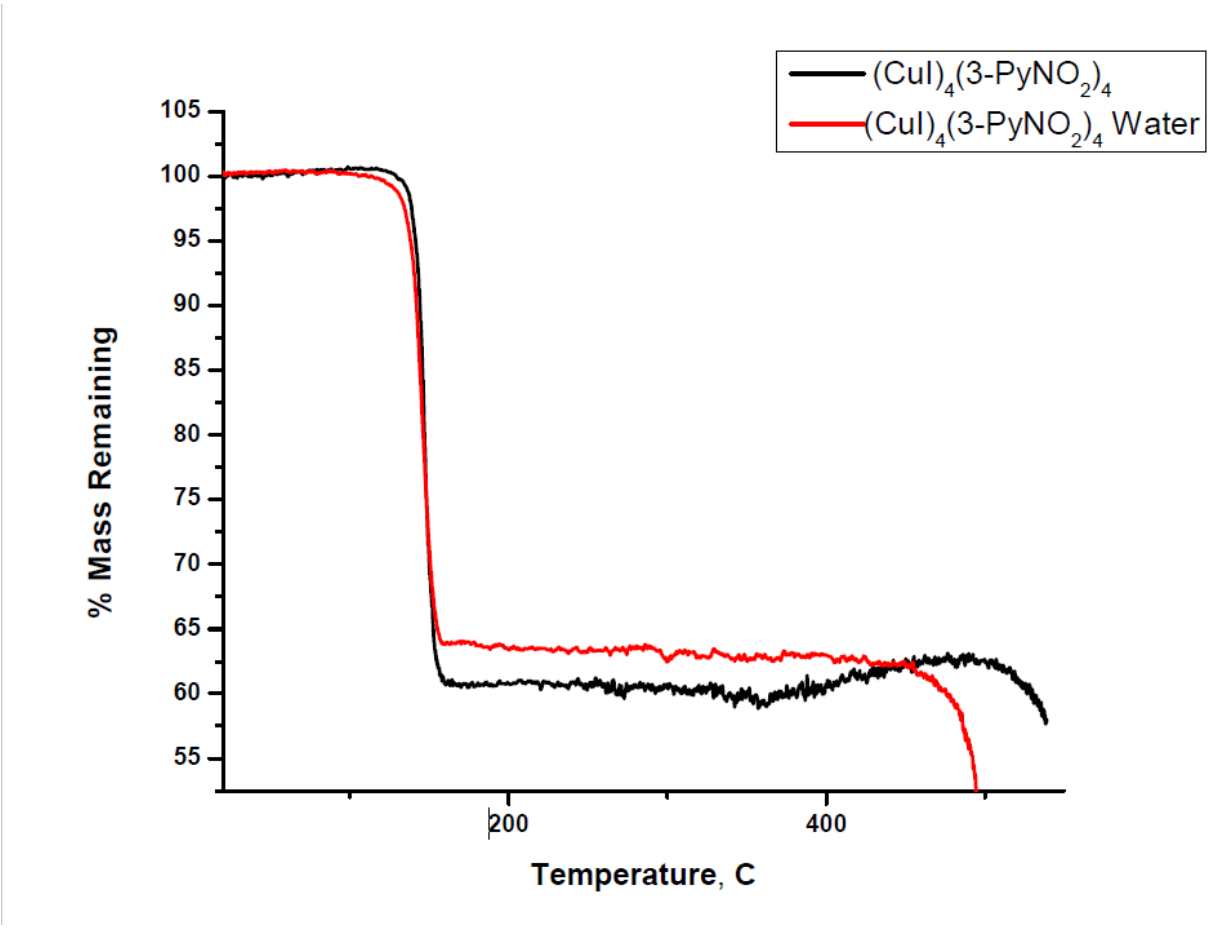

Figure 5.5: TGA of **7** before and after 24 h in water at RT

The sample exposed to water clearly had less ligand to lose than the pure material. Furthermore, the difference is significant enough to be clearly observable via TGA. A loss of this much ligand is a very reasonable amount to correspond to the amount of ligand readily available on the surface of the material. It suggests quite strongly that the complex is not entirely stable in water.

The work discussed in Chapter 1 of this work theorized that the reorganization of CuI was the rate determining step in vapochromic reactions. The extension of this result was our attempt to increase reaction rate by using a preformed exchange compound, **7**. The results from the aqueous testing show very little to separate CuI from the exchange compound in speed of reaction. This result is surprising even with the extension from gas/solid to liquid/solid. A

reasonable explanation for this behavior is that the water solubility of 3-$PyNO_2$, the ligand of **7,** is presenting a problem. The intentionally weakly bound ligand could easily be pulled from the surface by water. This would trigger a reorganization of the material at the surface to resemble γ-CuI. Therefore the primary site of reaction for both complexes (the surface) would be quite similar chemically. From this point the two would share a reaction mechanism whereby the CuI surface is reorganized into the pyridine cubane, much as described above in Chapter 1. This proposed system is described below, in Scheme 5.2.

Scheme 5.2: Proposed mechanism of the reaction of **7** in aqueous pyridine

$(CuI)_4(3\text{-}PyNO_2)_4$ (surface) + H_2O → $(CuI)_4$ (cubane) + 4 3-$PyNO_2$ (aq)

$(CuI)_4$ (cubane) → γ-CuI

γ-CuI + Py → $(CuI)_4(Py)_4$ (cubane)

This mechanism is dissociative in nature and so is supportive of the computational findings that a 5 coordinate copper(I) atom is highly unfavorable. Further, this explains the similarities in behavior between CuI and **7** in the DI water blank scan. Even in DI water the exchange compound would have surface ligand stripped off to return the surface to CuI. Unfortunately the exchange compound chosen appears to have no advantage over CuI in the realm of aqueous testing.

6) Future Work

CuI and the exchange compound showed preliminary promise as chemical sensing materials in water. The reactivity with pyridine was clearly observed in both, but the two different materials were very similar in performance. The possibility of using either **7** or some other CuI based material to detect gas phase compounds is promising. The work discussed in Chapter 1 suggested a strong benefit for removing the rearrangement step of the vapochromic reaction. The low volatility and weak binding of **7** make it a strong candidate moving forward for gas phase testing. It is worth considering other materials as well to help confront the relatively high cost of the nitropyridine ligand. To further test aqueous conditions, a new material needs to be developed. Ideally this material would share some of the characteristics of 3-$PyNO_2$ like weak binding and

no/minimal emission with lower solubility in water. It may be a more aliphatic ligand would be a better option for this type of testing. Even CuI itself has some promise in these avenues, and its performance could be increased by modifying its non-chemical properties like particle size. The low cost, ready availability, and generally straightforward synthetic chemistry of CuI make it a strong base material to build chemical sensors off of.

Bibliography:

1) Stefels, J., Steinke, M., Turner, S., Malin, G., & Belviso, S. (2007). Environmental constraints on the production and removal of the climatically active gas dimethylsulphide (DMS) and implications for ecosystem modelling. *Biogeochemistry*, *83*(1–3), 245–275. https://doi.org/10.1007/s10533-007-9091-5
2) Rahman, M. A., Kumar, P., Park, D. S., & Shim, Y. B. (2008). Electrochemical sensors based on organic conjugated polymers. *Sensors*, *8*(1), 118–141. https://doi.org/10.3390/s8010118
3) Kodavanti, P. R. S. (2005). Neurotoxicity of Persistent Organic Pollutants: Possible Mode(S) of Action and Further Considerations. *Dose-Response*, *3*(3), dose-response.0. https://doi.org/10.2203/dose-response.003.03.002
4) Stetter, J. R., Penrose, W. R., & Yao, S. (2003). Sensors, Chemical Sensors, Electrochemical Sensors, and ECS. *Journal of The Electrochemical Society*, *150*(2), S11. https://doi.org/10.1149/1.1539051
5) Report, A. (2020). Field Portable Gas Chromatograph Mass Spectrometers Assessment Report. *Ael*, *07CD-01-DP*(February). Retrieved from https://www.dhs.gov/sites/default/files/saver-gcms_assessment_report_05feb2020-508.pdf%0Ahttps://www.dhs.gov/science-and-technology/frg-publications#
6) Ritter, L., Solomon, K. ., & Forget, J. (2011). Persistent Organic Pollutants - An Assessment Report on: DDT-Aldrin-Dieldrin-Endrin-Chlordane-Heptachlor-Heptachlorobenzene-Mirex-Tozapene-Polychlorinated Biphenyls-Dioxins and Furans. *Chemosphere*, 43 pp.
7) Demas, J. N., Degraff, B. A., & Madison, J. (2001). Applications of luminescent transition platinum group metal complexes to sensor technology and molecular probes. *Coord. Chem. Rev.*, *211*, 317–351.
8) Shahjamali, M. M., Salvador, M., Bosman, M., Ginger, D. S., & Xue, C. (2014). Edge-Gold-Coated Silver Nanoprisms: Enhanced Stability and Applications in Organic Photovoltaics and Chemical Sensing. *J. Phys. Chem. C*, *118*, 12459–12468. https://doi.org/10.1021/jp501884s
9) Zhang, B., & Gao, P. (2019). Metal Oxide Nanoarrays for Chemical Sensing : A Review of Fabrication Methods , Sensing Modes , and Their. *Front. in Mater.*, *6*(April). https://doi.org/10.3389/fmats.2019.00055
10) Comini, E., & Sberveglieri, G. (2010). Metal oxide nanowires It is almost a decade since the first presentation of metal oxide nanowires. *Materials Today*, *13*(7–8), 36–44. https://doi.org/10.1016/S1369-7021(10)70126-7
11) Kreno, L. E., Leong, K., Farha, O. K., Allendorf, M., Duyne, R. P. Van, & Hupp, J. T. (2012). Metal À Organic Framework Materials as Chemical Sensors. *Chem. Rev.*, *112*, 1105–1125. https://doi.org/10.1021/cr200324t
12) Lee, W. S., & Choi, J. (2019). Hybrid Integration of Carbon Nanotubes and Transition Metal Dichalcogenides on Cellulose Paper for Highly Sensitive and Extremely Deformable Chemical Sensors. *ACS Appl. Mater. Interfaces*, *11*, 19363–19371. https://doi.org/10.1021/acsami.9b03296
13) Skotadis, E., Tanner, J. L., Stathopoulos, S., Tsouti, V., & Tsoukalas, D. (2012). Sensors and Actuators B : Chemical Chemical sensing based on double layer PHEMA polymer and platinum nanoparticle films. *Sensors & Actuators: B. Chemical*, *175*, 85–91. https://doi.org/10.1016/j.snb.2011.12.058

14) Ford, P. C., Cariati, E., & Bourassa, J. (1999). Photoluminescence Properties of Multinuclear Copper (I) Compounds. *Chem. Rev.*, *99*(I), 3625–3647.
15) Mourzina, Y. G., Schöning, M. J., Schubert, J., Zander, W., Legin, A. V, Vlasov, Y. G., & Lüth, H. (2001). Copper , cadmium and thallium thin film sensors based on chalcogenide glasses. *Anal. Chim. Acta*, *433*, 103–110.
16) Wang, G., Gu, A., Wang, W., Wei, Y., Wu, J., Wang, G., … Fang, B. (2009). Electrochemistry Communications Copper oxide nanoarray based on the substrate of Cu applied for the chemical sensor of hydrazine detection. *Electrochemistry Communications*, *11*(3), 631–634.
17) Pal, S. K. (2011). Copper Quantum Clusters in Protein Matrix : Potential Sensor of. *Anal. Chem.*, 9676–9680.
18) Angelis, F. De, Fantacci, S., Sgamellotti, A., Cariati, E., Ugo, R., Ford, P. C., … Uni, V. (2006). Electronic Transitions Involved in the Absorption Spectrum and Dual Luminescence of Tetranuclear Cubane [Cu_4I_4 (pyridine)$_4$] Cluster : a Density Functional Theory / Time-Dependent Density Functional Theory Investigation. *Inorg. Chem.*, *45*(26), 10576–10584.
19) Das, N. K., Ghosh, S., Priya, A., Datta, S., & Mukherjee, S. (2015). Luminescent Copper Nanoclusters as a Specific Cell-Imaging Probe and a Selective Metal Ion Sensor. *J. Phys. Chem. C*, *119*, 24657–24664.
20) Bowmaker, G. A., Kennedy, B. J., & Reid, J. C. (2006). Crystal Structures of AuCN and AgCN and Vibrational Spectroscopic Studies of AuCN ,. *Inorg. Chem.*, *1669*(97), 3968–3974.
21) Matebese, F., Taziwa, R., & Mutukwa, D. (2018). Progress on the Synthesis and Application of CuSCN Inorganic Hole Transport Material in Perovskite Solar Cells. *Materials*, *11*, 2592.
22) Cariati, E., Bu, X., & Ford, P. C. (2000). Solvent- and Vapor-Induced Isomerization between the Luminescent Solids [CuI (4-pic)]$_4$ and [CuI (4-pic)] ∞ (pic) methylpyridine). The Structural Basis for the Observed Luminescence Vapochromism. *Chem. Mater.*, (6), 3385–3391.
23) SADABS: Bruker Analytical X-ray Systems: Madison, WI, 2001.
24) G. M. Sheldrick, Acta Crystallogr., Sect. A. 64 (2008) 112
25) Welch, D. A.; Woehl, T. J.; Park, C.; Faller, R.; Evans, J. E.; Browning, N. D. Understanding the Role of Solvation Forces on the Preferential Attachment of Nanoparticles in Liquid. *ACS Nano* **2016**, *10* (1), 181–187.
26) Bussi, G.; Donadio, D.; Parrinello, M. Canonical Sampling Through Velocity Rescaling. *J. Chem. Phys.* **2007**, *126* (1), 014101.
27) Killarney, J. P., Mckinnon, M., Murphy, C., Henline, K. M., Wang, C., Pike, R. D., & Patterson, H. H. (2014). Amine- and sulfide-sensing copper (I) iodide films. *INOCHE*, *40*, 18–21.
28) Varju, B. R.; Ovens, J. S.; Leznoff, D. B. Mixed Cu(I)/Au(I) Coordination Polymers as Reversible Turn-On Vapoluminescent Sensors for Volatile Thioethers. *Chem. Commun.* **2017**, *53* (48), 6500–6503.
29) Lefebvre, J.; Batchelor, R. J.; Leznoff, D. B. $Cu[Au(CN)_2]_2(DMSO)_2$: Golden Polymorphs That Exhibit Vapochromic Behavior. *J. Am. Chem. Soc.* **2004**, *126* (49), 16117–16125.
30) Perruchas, S., Le, X. F., Fargues, A., Garcia, A., & Kahlal, S. (2011). Thermochromic Luminescence of Copper Iodide Clusters : The Case of Phosphine Ligands. *Inorg. Chem.*, *50*, 10682–10692.
31) Taylor, W. V, Cammack, C. X., Shubert, A., & Rose, M. J. (2019). Thermoluminescent Antimony-Supported Copper-Iodo Cuboids: Approaching NIR Emission via High Crystallographic Symmetry. *Inorg. Chem.*, *58*, 16330–16345.

32) Humphrey, W.; Dalke, A.; Schulten, K. VMD: Visual Molecular Dynamics. *J. Mol. Graph.* **1996**, *14* (1), 33–38.
33) Alcock, N. W.; Benton, D. J.; Moore, P. Kinetics of Series First-Order Reactions. Analysis of Spectrophotometric Data by the Method of Least Squares and an Ambiguity. *Trans. Faraday Soc.* **1970**, *66*, 2210.
34) Tatsuya Hasegawa, Atsushi Kobayashi, Hiroki Ohara, Masaki Yoshida, and Masako Kato. *Inorganic Chemistry* **2017** *56* (9), 4928-4936
35) X.-C. Huang, S. W. Ng, *Acta Cryst.* E60 (2004) m1055.
36) E. Cariati, D. Roberto, R. Ugo, P.C. Ford, S. Galli, A. Sironi, *Inorg. Chem*. 44 (2005) 4077.
37) F. Gschwind, O. Sereda, K.M. Fromm, Inorg. Chem. 48 (2009) 10535; (b) P.C. Healy, C. Pakawatchai, C.L. Raston, B.W. Skelton, A.H. White, *J. Chem. Soc., Dalton Trans*. (1983) 1905.
38) A.J. Graham, P.C. Healy, J.D. Kildea, A.H. White, Aust. J. Chem. 42 (1989) 177
39) S. Jana, K. Harms, S. Chattopadhyay, *J. Iran Chem. Soc.* 13 (2016) 1713
40) M.K. Broderick, C. Yang, R.D. Pike, A. Nicholas, D. May, H.H. Patterson, *Polyhedron* 114, (2016) 333.
41) E. Cariati, D. Roberto, R. Ugo, P.C. Ford, S. Galli, A. Sironi, *Inorg. Chem*. 44 (2005) 4077.
42) S.-Y. Yin, Z. Wang, Z.-M. Liu, H.-J. Yu, J.-H. Zhang, Y. Wang, R. Mao, M. Pan, C.-Y. Su, Inorg. Chem. 58 (2019) 10736Volz, D., Zink, D. M., Bocksrocker, T., Friedrichs, J., Nieger, M., Baumann, T., … Bra, S. (2013). Molecular Construction Kit for Tuning Solubility, Stability and Luminescence Properties: Heteroleptic MePyrPHOS-Copper Iodide- Complexes and their Application in Organic Light-Emitting Diodes. *Chem. Mater.*, *25*, 3414–3426.
43) W. Liu, Y. Fang, G.Z. Wei, S.J. Teat, K. Xiong, Z. Hu, W.P. Lustig, Jing Li, J. Am. Chem Soc. 137 (2015) 9400
44) Schlachter, A., Viau, L., Fortin, D., Knauer, L., Strohmann, C., Knorr, M., & Harvey, P. D. (2018). Control of Structures and Emission Properties of (CuI). *Inorg. Chem.*, *57*, 13564–13576.
45) Sun, X., Wang, Y., & Lei, Y. (2015). Fluorescence based explosive detection: From mechanisms to sensory materials. *Chemical Society Reviews*, *44*(22), 8019–8061.